広島大学学位請求論文

Establishment of a novel method for visualization of calcium dynamics and evaluation of epidermal barrier function using human skin tissue

（ヒト皮膚組織を用いた表皮カルシウム動態の可視化とバリア機能評価の新手法確立）

２０２０年

広島大学大学院理学研究科

数理分子生命理学専攻

熊本　淳一

北海道大学電子科学研究所

附属社会創造数学研究センター 人間数理研究分野 学術研究員

JST　科学技術振興機構　CREST 研究員

目　次

1. 主論文

Establishment of a novel method for visualization of calcium dynamics and evaluation of epidermal barrier function using human skin tissue
（ヒト皮膚組織を用いた表皮カルシウム動態の可視化とバリア機能評価の新手法確立）
熊本　淳一

2. 公表論文

(1) Japanese Cedar (*Cryptomeria japonica*) pollen allergen induces elevation of intracellular calcium in human keratinocytes and impairs epidermal barrier function of human skin ex vivo. Kumamoto J., Tsutsumi M., Goto M., Nagayama M., Denda M. Archives of Dermatological Research, 308, 2016, 49-54.

(2) Real-time imaging of human epidermal calcium dynamics in response to point laser stimulation. Kumamoto J., Goto M., Nagayama M., Denda M. Journal of Dermatological Science, 86, 2017, 13-20.

(3) Mathematical-model-guided development of full-thickness epidermal equivalent. Kumamoto J., Nakanishi S., Makita M., Uesaka M., Yasugahira Y., Kobayashi Y., Nagayama M., Denda S., Denda M. Scientific Reports, 17999, 2018, 8.

(4) Frontiers in epidermal barrier homeostasis - an approach to mathematical modelling of epidermal calcium dynamics. Denda M, Denda S, Tsutsumi M, Goto M, Kumamoto J, Nakatani M., Takei K., Kitahata H., Nakata S., Sawabu Y., Kobayashi Y., Nagayama M. Experimental Dermatology, 23, 2014, 79-82.

3. 参考論文

(1) External negative electric potential accelerates exocytosis of lamellar bodies in human skin *ex vivo*. Kumamoto J., Goto M., Denda S., Nakatani M., Takasugi Y., Tsuchiya K., Shimizu Y., Takatsuru Y., Denda M. Experimental Dermatology, 22, 2013, 1-3.

主論文

Establishment of a novel method for visualization of calcium dynamics and evaluation of epidermal barrier function using human skin tissue

（ヒト皮膚組織を用いた表皮カルシウム動態の可視化とバリア機能評価の新手法確立）

Table of Contents

Abbreviations 4
Chapter 1. General Introduction 5
1-1. Backgrounds 5
1-2. Aim of this work 9
1-3. Figures 10
Chapter 2. External negative electric potential accelerates exocytosis of lamellar bodies in human skin *ex vivo* 13
2-1. Introduction 13
2-2. Materials and methods 15
2-3. Results 17
2-4. Discussion 18
2-5. Figures 20
Chapter 3. Japanese Cedar (*Cryptomeria japonica*) pollen allergen induces elevation of intracellular calcium in human keratinocytes and impairs epidermal barrier function of human skin ex vivo 23
3-1. Introduction 23
3-2. Materials and methods 24
3-3. Results 27
3-4. Discussion 29
3-5. Figures 30
Chapter 4. Real-time imaging of human epidermal calcium dynamics in response to point laser stimulation 34
4-1. Introduction 34
4-2. Materials and methods 35
4-3. Results 38
4-4. Discussion 40
4-5. Figures 43
Chapter 5. Mathematical-model-guided development of full-thickness epidermal equivalent 49
5-1. Introduction 49
5-2. Materials and methods 51
5-3. Results 55

5-4. Discussion 57
5-5. Figures 59
Chapter 6. General Conclusion 76
Acknowledgments 80
References 81

Abbreviations

4α-PDD = 4α-phorbol 12,13-didecanoate
AD = Atopic dermatitis
ATP = Adenosine triphosphate
BrdU = Bromodeoxyuridine
BSS = Balanced salt solution
CTR = Cell Tracker™ Red CMTPX
Cry j1 = *Cryptomeria japonica* 1
FSY-NH2 = FSLLRY-NH2
GPCR = G protein-coupled receptor
HE = Hematoxylin-Eosin
ICAM-1 = Intercellular adhesion molecule 1
IL = Interleukin
IgE = Immunoglobulin E
IP3 = Inositol trisphosphate
K14 = Keratin 14
LTSCM = Long term skin culture medium
MCSP = Melanoma-associated chondroitin sulfate proteoglycan
OG = Oregon Green™ 488 BAPTA-1
PAR = Protease activated receptor
PFA = Paraformaldehyde
SB = Stratum basale
SBTI = Soybean trypsin inhibitor
SC = Stratum corneum
SG = Stratum granulosum
SS = Stratum spinosum
TEWL = Trance epidermal water loss
TRP = Transient receptor potential
YAP = Yes-associated protein

Chapter 1. General Introduction

1-1. Backgrounds

The skin, which is the body's largest organ, consists of three layers, epidermis, dermis, and fat layer, and contains a great many structures, including nerve fibers, sebaceous glands, hair follicles, and capillaries (Figure 1-1). The epidermis, the outermost layer of the skin, is very thin, with a thickness of about 0.2 μm, and is composed of four layers: stratum corneum (SC), stratum granulosum (SG), stratum spinosum (SS), and stratum basale (SB), which consist mostly of keratinocytes.

Keratinocytes are generated at the lowest layer of the epidermis and differentiate as they move towards the skin surface. In the SG, the uppermost layer of the living epidermis, lipid-containing granules, known as lamellar bodies, appear, and the lipids are secreted into the intercellular region to form lamellar structures at the final stage of differentiation. Finally, the SC is formed by secreted lipids and nucleated keratinocytes, serving as a water-impermeable barrier (1). It is important that the function of this water-impermeable barrier is constantly maintained in order to prevent excessive water loss from the body and to protect the body from environmental insults, such as physicochemical stimuli and microorganisms, including viruses.

Calcium ions in the epidermis play a key role in maintaining the barrier function. The calcium ion concentration in the epidermis of healthy subjects shows a characteristic gradient, being low in the SS and SB, high in the SG, and low again in the SC (2) (Figure 1-2). Therefore, the surface of the skin has a negative electric potential with reference to the bottom of the epidermis (3, 4). When the barrier function is destroyed by tape stripping or acetone treatment, the secretion of lipids from the lamellar granules is accelerated immediately after the disruption, and lipid synthesis is increased, leading to restoration of the barrier function (1). In addition, when the barrier function is lost, both the calcium gradient and the electric potential disappear, while both return to their original levels when the barrier function is fully recovered. Covering the skin with a water-impermeable membrane, such as cling film, after barrier breakdown not only blocks the barrier recovery, but also prevents re-formation of the calcium gradient and the negative potential of the skin (5). Thus, changes of skin surface electric potential and calcium dynamics might represent two sides of the same coin.

Calcium pumps and channels in epidermal cells play important roles in maintaining the calcium ion concentration and skin surface potential. Mutations in the calcium pump

are associated with abnormal differentiation of keratinocytes and hereditary skin diseases with impaired barrier function (6, 7). Calcium pump and calcium channel agonists affect the potential of the skin surface (4, 8). Notably, Denda *et al.* demonstrated that a variety of neurotransmitters and receptors first discovered in the brain are also expressed in keratinocytes, and that chemical regulation of these molecules affects barrier homeostasis (9-15). Interestingly, the nervous system is regulated by calcium dynamics and changes in the electrophysiological state of cell membranes induced by other ions through neurotransmitter receptors. In other words, barrier function and homeostasis appear to be regulated by ion dynamics in a manner similar to that in the nervous system. However, the mechanisms that control calcium ion dynamics are still incompletely understood, especially in human skin tissue.

Allergens are known to lower the epidermal barrier function. Allergic reactions due to pollinosis and food are usually caused by the binding of antigenic proteins (allergens) to IgE antibodies previously formed on the FcεRI high affinity receptor present on the surface of mast cells. Antigen binding to the IgE antibody induces release of chemical mediators such as histamine stored in granules in mast cells, as well as causing secretion of leukotrienes and cytokines. These mediators promote the inflammatory response (16).

The protease-activated receptors (PARs), which belong to the G protein-coupled receptor (GPCR) family, play a role in the development of many chronic inflammatory diseases. There are four types of PAR: PAR-1 to PAR-4. PAR-1, PAR-3 and PAR-4 are activated by thrombin, and PAR-2 is activated by trypsin, mast cell tryptase, and coagulation factors VIIa/Xa. Activation of PARs involves proteolytic cleavage of the extracellular N terminus of the receptor by serine proteinases, revealing a new N-terminal amino acid sequence that interacts with the second extracellular loop of the receptor to stimulate G protein and β-arrestin-dependent signaling. PARs other than PAR-3 can also be activated by an oligopeptide consisting of 5 to 7 amino acids matching the amino acid sequence of the tether ligand (17).

PAR-2 is expressed in multiple organs, tissues and cells, and has many physiological roles, including in the circulatory system, respiratory system, and central nervous system. It is also expressed in the epidermis, mainly in the SB and SG (18). PAR-2 activation of keratinocytes plays an important role in inflammatory diseases via release of IL-8 cytokine and increased melanin uptake by melanocytes (18, 19).

A particularly common allergy in Japan is pollinosis. In particular, approximately 25 % of the population suffers from cedar pollinosis (20). There are many types of cedar pollen allergens, but among them, Cry j1 is thought to be the major allergen. Cry j1 is a

basic protein with a molecular weight of about 40 kDa, and is localized in Bish bodies (about 0.7 μm in diameter) attached to the surface of cedar pollen, which has a diameter of about 30 μm (21, 22). Mite, cockroach and house dust allergens activate PAR-2 in epidermal keratinocytes and delay epidermal permeability barrier recovery after disruption (23, 24), but it has not been established whether cedar pollen delays barrier recovery via a similar mechanism.

The traditional view of the skin surface sensory systems for environmental factors, such as temperature, humidity, mechanical stress and chemical stimuli, has been that the key sensors are C fibers, which penetrate into the epidermis (25), but the terminals of these nerve fibers are quite sparse. For example, the pressure points, which detect mechanical stimuli, are localized at distances of millimeter order from each other (26). However, the skin can detect pattern on a much smaller scale (27-30) than would be expected on the basis of sampling theory if the nerve terminals were the only sensors (31). Instead, Denda *et al*. proposed that epidermal keratinocytes might be at the forefront of skin sensory perception (32). Indeed, many receptors for many environmental factors are expressed on keratinocytes. For example, transient receptor potential (TRP) receptors act as sensors of temperature and other physical or chemical factors (33). Among the TRP channel family members, TRPV1 and TRPV2, TRPV3, TRPV4, TRPM8, TRPA1 are expressed in keratinocytes (34-36).

TRPV1 is activated by heat above 43 ºC, acidic conditions (pH < 6.6), or capsaicin (37). TRPV3 is activated by heat above 35 ºC or mechanical stimulation (38, 39). TRPV4 is activated by heat at 30 ºC to 40 ºC, 4α-phorbol 12,13-didecanone (4α-PDD), an agonist of TRPV4, and also by osmotic pressure (33). Denda *et al*. demonstrated that TRPV1 and TRPV4 are closely related to barrier function homeostasis (40). Activation of TRPV1 by heat (around 43 ºC) or capsaicin after barrier disruption delayed barrier repair. This delay in barrier recovery is inhibited by capsazepine, a TRPV1 antagonist. On the other hand, activation of TRPV4 by heat (36 ºC to 40 ºC) accelerates barrier recovery. These results suggest that the TRP receptors play an important role in barrier homeostasis.

The ATP receptor also plays an important role in responses to environmental factors and barrier homeostasis. The nervous system contains two distinct families of ATP receptors (41). One is the ATP-activated purinergic receptor (P2X) family, which consists of ligand-gated ion channels, and the other is the P2Y family of metabotropic, heptahelical G-protein-coupled receptors. The P2X3 receptor, a member of the P2X family, was first identified as a pain receptor in the peripheral nervous system (42). In response to tissue injury or inflammation, ATP is released and P2X3 receptors are

activated. Denda *et al.* found that the P2X3 receptor is highly expressed in the upper area of the epidermis (43, 10). Not only P2X3, but also other P2X and P2Y receptors are expressed in epidermal keratinocytes (43, 44). P2X3 in epidermal keratinocytes is associated with barrier homeostasis (10). Koizumi *et al*. demonstrated that mechanical stimulation of a single keratinocyte induced intracellular calcium elevation not only in that cell, but also in its neighbors, and this response was prevented by application of an ATP receptor blocker (44). They obtained similar results in a keratinocyte-nerve co-culture system, and found that mechanical stimulation of a single keratinocyte induced excitation of neurons (44). Thus, a single keratinocyte that receives mechanical stimulation can transmit a signal to surrounding cells, and induce excitation of the peripheral nervous system. The diffusion of ATP induces additional intracellular calcium elevation, which might be the cause of calcium waves. Denda *et al.* demonstrated that ATP receptor inhibitors block intracellular calcium transmission in keratinocytes (45). Thus, ATP plays an important role in signaling among keratinocytes.

Slominski *et al.* suggested that cutaneous endocrine systems not only transduce signals within the skin, but are also involved in skin-nerve or skin-endocrine communication. The interaction between the skin and the neuroendocrine system might influence the immune, vascular, metabolic, thermoregulatory and sensory systems (46-49). Overall, a detailed understanding of the interactions between keratinocytes and the nervous system, as well as the communication pathways among keratinocytes, should throw light on the nature of the epidermis as a multi-sensory organ and its role in barrier homeostasis.

Traditional research on dermatology has mainly been based on biochemical or molecular-biological approaches. However, a mathematical approach is also effective in understanding macroscopic behavior, such as epidermal homeostasis. Indeed, many mathematical models of the epidermis have been proposed so far, including a lattice model of stochastic cell dynamics (50) and a particle dynamics model to explain tumor growth (51), as well as particle-based models of skin structure (52-54). However, the SC has a flattened shape, in contrast to the cells forming the living epidermis. Therefore, in order to understand SC barrier function, it is important to monitor spatiotemporal changes in the structure of the SC.

Cornelissen and Adams have mathematically modeled calcium localization in the epidermis (55,56), but it is unclear how this is related to the structure of the epidermis. Grabe and Neuber used a particle-based model that considered calcium ions to simulate the structure of the epidermis and recreate a flat epidermal surface (57). Mathematical models rarely consider the mechanism of SC formation. However, Kobayashi *et al.*

proposed a particle-based mathematical model of epidermis incorporating calcium dynamics and demonstrated that epidermal homeostasis can be maintained with the help of calcium dynamics (Figure 1-3). This model is composed of keratinocytes generated from stem cells distributed in the stratum basale; it incorporates not only cell-cell interaction, but also dynamic cellular processes of the epidermis, such as intracellular calcium ion dynamics and cell differentiation. Simulation of epidermal homeostasis has been performed using the mathematical model (58-60).

Thus, mathematical techniques can be used to model not only individual biological functions, but also the entire system as a hierarchical structure. However, although many mathematical models of known dermatological phenomena have been constructed, there are few examples of mathematical model-based predictions of biological behaviour that have subsequently been verified by means of biochemical and molecular-biological studies.

1-2. Aim of this work

The aim of this doctoral dissertation is to establish of new methods for visualization of calcium dynamics and evaluation of epidermal barrier function using human skin tissue by combining physiological experiment and mathematical models. Specifically, the following four studies were conducted.

In chapter 2, I examine the hypothesis that the potential of the epidermal surface might affect the secretion of lamellar granules that make up the barrier. To test this idea, a negative potential was applied to human skin tissue, and the ultrastructure of the uppermost layer was observed.

In Chapter 3, I aim to establish a barrier function evaluation method using human skin tissue, and investigate the effect of Cry j1, a major allergen causing cedar pollinosis in Japan, on epidermal barrier function and examine the role of PAR-2 in its action.

In Chapter 4, in order to understand the calcium dynamics associated with epidermal barrier homeostasis, I develop and apply a novel method for real-time measurement of calcium dynamics in response to point stimulation of human skin tissue at the single-cell level.

In Chapter 5, I use computer simulations based on a mathematical model of epidermal homeostasis to predict how to build epidermal equivalent models with high barrier function, including experimental validation of the predictions.

1-3. Figures

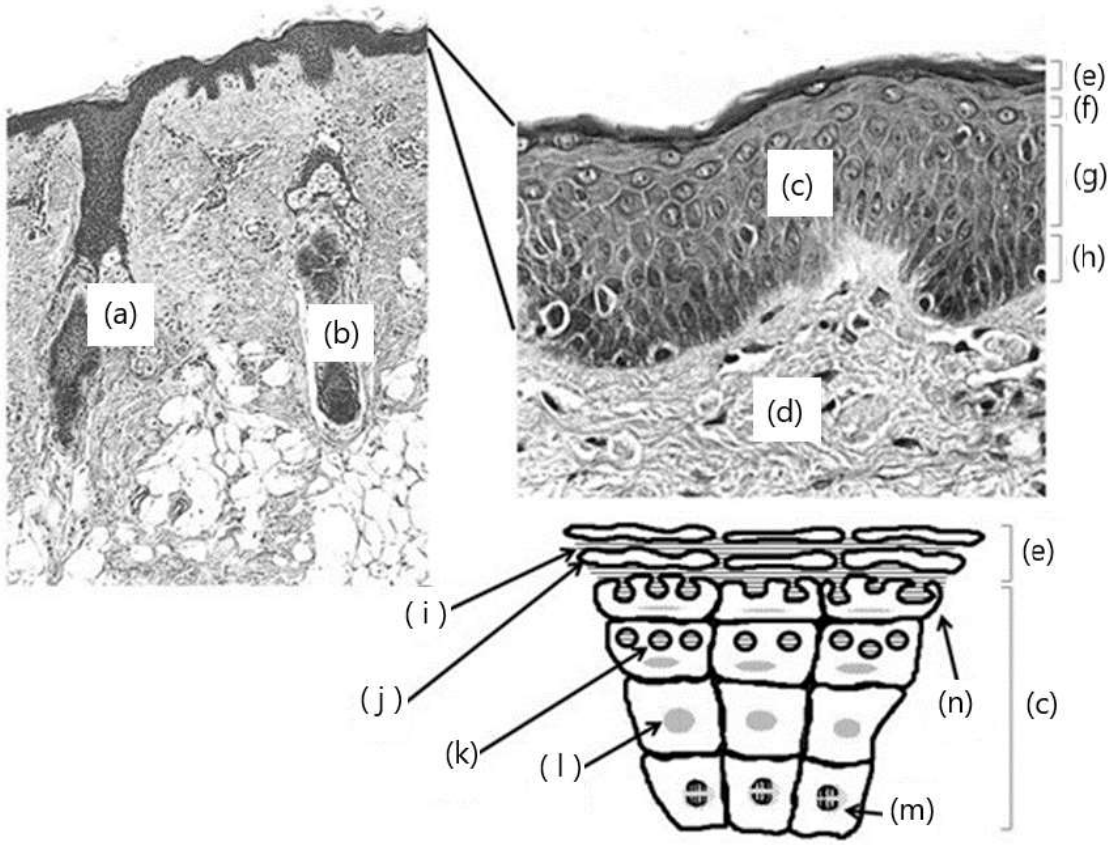

Figure 1-1.
Structure of skin and mechanism of lamellar granule secretion

(a) Sebaceous gland
(b) Hair follicle
(c) Epidermis
(d) Dermis
(e) Stratum corneum (SC)
(f) Stratum granulosum (SG)
(g) Stratum spinosum (SS)
(h) Stratum basale (SB)
(i) Intercellular lipid
(j) Cornified keratinocytes
(k) Lamellar granules
(l) Nucleus
(m) Stem cell
(n) Exocytosis

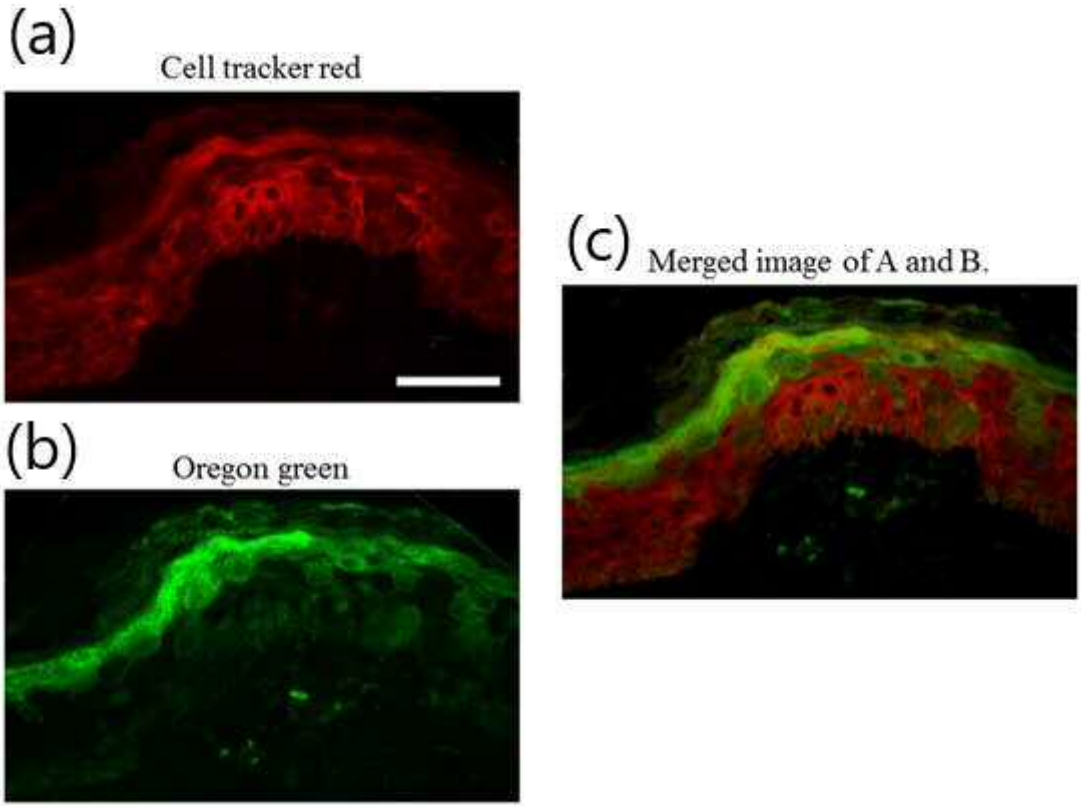

Figure 1-2.

Calcium localization at the uppermost layer of human skin tissues. (a) Live cells were stained with Cell Tracker (Red colour). (b) Calcium ion was stained with Oregon green. (c) Merged image of a and b. Bar = 50 μm.

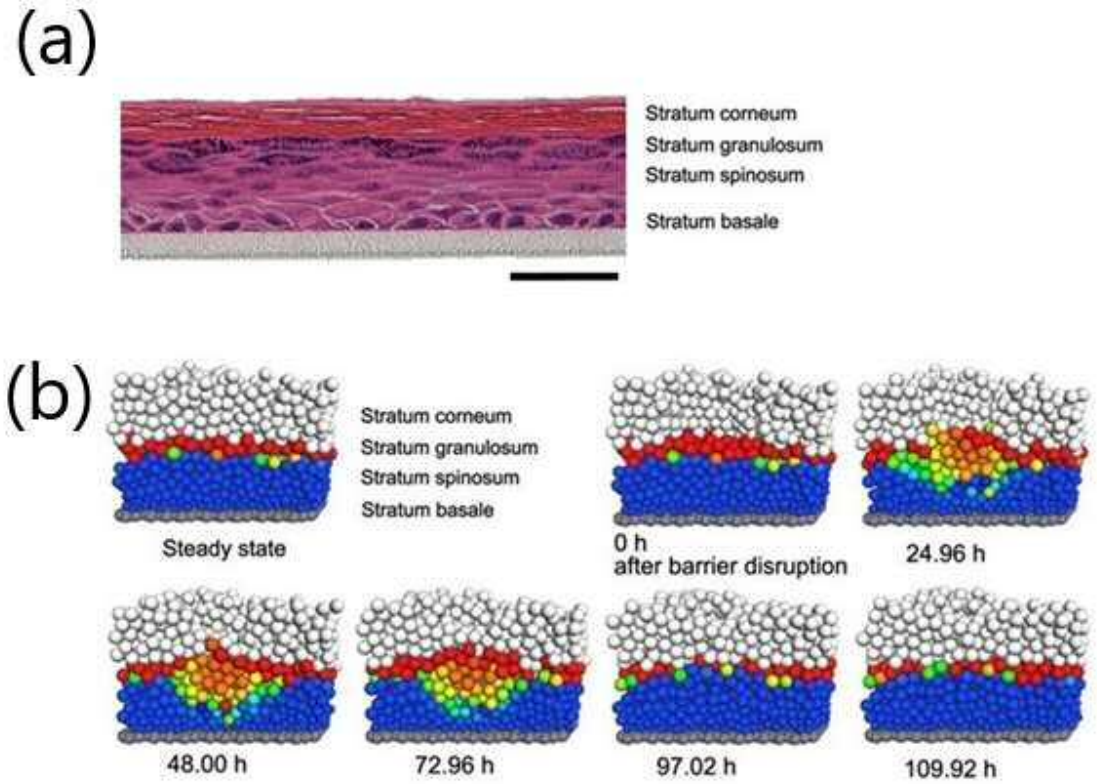

Figure 1-3.

(a) Epidermal-equivalent model (hematoxylin and eosin (H&E) staining) Bar = 50 μm. (b) Computer simulation of the time course of barrier recovery after disruption, using a particle-based mathematical model of the epidermis incorporating calcium dynamics. White: stratum corneum. Intracellular calcium levels are shown in false colour, where blue, green, yellow and red indicate increasing intracellular calcium concentrations in that order. In the deepest layer, grey-coloured cells correspond to keratinocytes in the basal layer. Numbers under each illustration indicate the time after barrier disruption.

Chapter 2. External negative electric potential accelerates exocytosis of lamellar bodies in human skin *ex vivo*

2-1. Introduction

One of the most important roles of the skin is to generate a water-impermeable barrier to excessive transdermal water loss. In skin diseases such as atopic dermatitis and psoriasis, this barrier function is reduced (61, 62).

This barrier function resides in the SC, which is the uppermost thin layer, and is composed of two components, i.e., protein-rich nonviable cells and intercellular lipid domains (63). When the barrier function of the SC is damaged by tape stripping or treatment with an organic solvent or detergent, a series of homeostasis processes in barrier function is immediately accelerated, and the barrier function recovers to its normal level (63). It is known that the localization of ions such as calcium and magnesium play an important role in the homeostasis of this barrier function (2, 64, 65, 66). Topical application of calcium chloride solution delays barrier function recovery after disruption of barrier function (64). On the other hand, it has been reported that a small amount of magnesium salt or mixture of magnesium and calcium salts accelerated the recovery of the barrier function for 3 hours after barrier damage (66). In normal skin, both calcium and magnesium were localized in the stratum granulosum (SG) of the uppermost layer of the epidermis, and the localization of calcium and magnesium disappears for 30 minutes after barrier disruption (2, 65). The normal skin surface has a negative potential against the inside, which decreases shortly after barrier disruption, and the recovery of this potential returns to the original level upon barrier recovery (67). Barker *et al.* suggested that this electric potential was caused by the living cell layer of the epidermis (3). Furthermore, Mitchell *et al.* suggested that alteration of ion localization changes the electric potential (68).

Denda *et al.* demonstrated that application of an external negative electric potential on hairless mouse skin accelerated recovery of the epidermal permeability barrier after disruption (69), and secretion of lamella granules was promoted in the intercellular lipid region between SC and SG after barrier destruction. Lamella granule secretion under the SC is a very important process for epidermal barrier homeostasis.

Based on these findings, I hypothesized that this potential might be a motive source of

lamella granule secretion, which is important for barrier formation. Then, in order to prove the process, the ultrastructure of the top layer of the human skin tissue after applying a negative potential (0.5 V) for 2 hours was observed.

2-2. Materials and methods

Human skin *ex vivo*

Human skin tissues were purchased from Biopredic International (Rennes, France) via KAC Co., Ltd. (Kyoto, Japan). They were obtained following plastic surgery, after informed consent had been obtained. The excised skin was dermatomed to 340-440 μm thickness (containing epidermis and dermis), punched into discs (12 mm in diameter), and then transferred to our laboratory. Samples of abdominal skin tissue from four healthy, independent subjects were used for the study. This study was approved by the ethics committee of Shiseido in accordance with the guideline of the National Institute of Health. Tissues were cultured with long-term skin culture medium (LTSC medium), provided by Biopredic International (Rennes, France).

Electron microscopic observation

Skin samples for electron microscopy was minced (< 0.5 mm^3 pieces) and fixed overnight in modified Karnovsky's fixative. They were then post-fixed in 2 % aqueous osmium tetroxide or 0.2 % ruthenium tetroxide). After fixation, all samples were dehydrated in graded ethanol solutions, and embedded in an Epon-epoxy mixture. The area of stratum corneum/stratum granulosum (SC/SG) lipid domain and the number of free lamellar bodies were quantified using osmium post-fixed material. Measurements were made without knowledge of the prior experimental treatment. These parameters were evaluated from photographs of randomly selected sections at constant magnification, using NIH Image software.

Two-photon laser-scanning microscopic observation of intercellular lipid

Skin discs were cultured with LTSC medium in an indium tin oxide-coated glass-based dish (ITO dish), provided by Dai Nippon Printing Co., Ltd. (Tokyo, Japan). Six skin discs were used for the study. Three skin discs were put on the ITO dish with the epidermis side up, then a platinum plate was placed on top of them, and a constant DC voltage (-0.5 V) was loaded on their surface by a function generator (Type19, Wavelike, Fort Worth, TX) for 2 h. No voltage was loaded on three control skin discs. Immediately thereafter, the skin discs were cut into 2x2 mm^2 pieces, which were incubated in LTSC medium containing 50 μg/ml Nile Red for 2 h. Samples were fixed with 4 % paraformaldehyde in PBS buffer solution for 1 h. These samples were cut in half and placed on a glass-bottomed dish. Each cross section faced the glass slide, so

that all layers of the epidermis could be observed in a single scan with a two-photon laser scanning microscope (A1R MP, Nikon, Tokyo, Japan) equipped with a Ti-sapphire laser, Mai Tai DeepSee (Spectra-Physics, California) and a x40 water immersion objective lens (N.A. = 1.15). The excitation wavelength was 810 nm and a 629/56 nm band pass filter was used for emission.

Two-photon laser-scanning microscopic observation of intracellular Ca^{2+}

Skin discs (6 mm in diameter) were cultured overnight in LTSC medium containing 20 μM Oregon Green 488 BAPTA-1, AM (OG). Then a constant voltage was loaded for 2 h, as described above. Immediately thereafter, the skin discs were observed under a two-photon laser scanning microscope (A1R MP, Nikon, Tokyo, Japan). Stratum corneum of each sample faced the glass slide. The excitation wavelength was 810 nm and a 525/50 nm band pass filter was used for emission. All 3D and 2D images were constructed from A1R MP images using NIS-Elements software (Nikon).

2-3. Results

The results of electron microscopic observation are shown in Figure 2-1, in which the intercellular lipid domain between the SC and SG can be seen. Exocytosis of a few lamellar bodies was observed in the osmium postfixed control skin (arrowheads). On the other hand, fusion of lamellar bodies was observed after application of negative potential (-0.5 V) for 2 h (Figure 2-1(b), asterisks). The results of quantification of the area of intercellular lipid domains are shown in Figure 2-1(c). The area of the domains was significantly increased by negative potential load, that is, exocytosis of lamellar bodies was accelerated.

To evaluate lipid structures in the SC/SG region, we observed ruthenium-stained skin. In control skin not exposed to electric potential, exocytosis was observed at several sites (Figure 2-1(d), arrowheads). On the other hand, fusion of secreted lamellar bodies was observed in skin after application of electric potential for 2 h (Figure 2-1(e, f)).

Denda *et al.* have reported that elevation of intracellular calcium accelerated lamellar body secretion (12). Moreover, the application of negative electric potential after barrier disruption increased the calcium ion gradient at the uppermost nucleated layer of the epidermis (69). In this study, I observed calcium ion gradation in the epidermis of control skin and potential-loaded skin by means of two-photon microscopy. The results are shown in Figure 2-2. There is a marked calcium gradient at the uppermost layer of the epidermis in the potential-loaded skin, as compared to the control skin.

I carried out two-photon microscopic observation to evaluate the structure of the intercellular lipid domains at the bottom layer of the SC. Intercellular lipid domains were observed in patches in control skin not exposed to potential load (Figure 2-3(a)), while continuous lipid domains were observed in skin after exposure to potential load (Figure 2-3(b)). Figure 2-3(c-g) show sliced images of the lipid domain of control skin at intervals of 1 μm. Images of 1 μm slices of skin after exposure to potential load are shown in Figure 2-3(h-l). Lipid domains can be seen more clearly in potential-loaded skin than in control skin. A three-dimensional image of the potential-loaded skin is shown in Figure 2-3(m). Broad lipid domains are apparent (arrow).

2-4. Discussion

In this study, I used human skin tissues *ex vivo* to exclude systemic effects. In agreement with previous findings in mice in vivo, both lamellar body exocytosis and fusion of secreted lipids were accelerated by electric potential loading. Moreover, in this study, I loaded the electric potential on untreated *ex vivo* skin, while in previous mouse study, I had loaded the potential after barrier disruption. Denda *et al.* suggested that external potential influenced lamellar body secretion during barrier recovery after disruption (69). On the other hand, this study suggest that lamella body exocytosis and the fusion of secreted lipids were regulated by the electrophysiological state of the epidermis even in skin where the barrier function is normally maintained.

The phase transition of lipids might be an important step in the secretion of lamella body and fusion of lipids into the intercellular domain, and the ionic environment could also be important for the phase transition of lipids. As reported by Denda *et al.* Increased intracellular calcium ion concentrations promoted lamellar body secretion after disruption of the epidermal barrier (12). Also, it has been shown that divalent cations such as Ca^{2+} and Mg^{2+} affected by phase transition in bilayers of charged lipids (70). Further, iontophoresis affected the epidermal calcium ion gradient in intact skin without disrupting the epidermal barrier (71). Changes in the ionic environment in the uppermost nucleated layer of the epidermis might influence phase transition in the lipid bilayer between lamella bodies and cell membrane or in the intercellular lipid domain between stratum corneum and stratum granulosum.

Lamellar body exocytosis in lung cells was accelerated by calcium influx (72, 73), and it was suggested that calcium ion channels might be involved in lamella granule secretion. Another study demonstrated that annexin II plays an important role in lamellar body fusion with plasma membrane, and this fusion was dependent on calcium ions (74). Annexin II is expressed in keratinocytes (75), and Denda *et al.* have also demonstrated that keratinocytes contain multiple calcium-permeable channels (76). Thus, annexin II or calcium ion channels might be involved in lamellar body secretion in the epidermis.

Denda *et al.* previously demonstrated that TRP channels were associated with epidermal barrier homeostasis (40, 77, 78). The balance of proteolytic activities might also be related to barrier homeostasis (79, 80). The relationship between the calcium gradient and those factors remains to be investigated. Denda *et al.* previously demonstrated that the electrical gradient was reduced by calcium ion pump blockers and calcium ion channel blockers (4), and suggested that maintenance of this gradient might

depend upon regulation of calcium dynamics by these pumps and channels. Denda *et al.* also showed that the calcium gradient and the electrical potential are closely related to each other (5). In normal skin, the calcium ion gradients play an important role in epidermal differentiation and epidermal permeability barrier homeostasis (81). The exocytosis of lamellar bodies is strongly associated with the calcium gradient (82), and a pH gradient is maintained by normal lamellar body secretion (83, 84).

Thus, the electrical potential and the calcium gradient can be seen as two sides of the same coin, and both might play key roles in various homoeostatic processes in the epidermis.

2-5. Figures

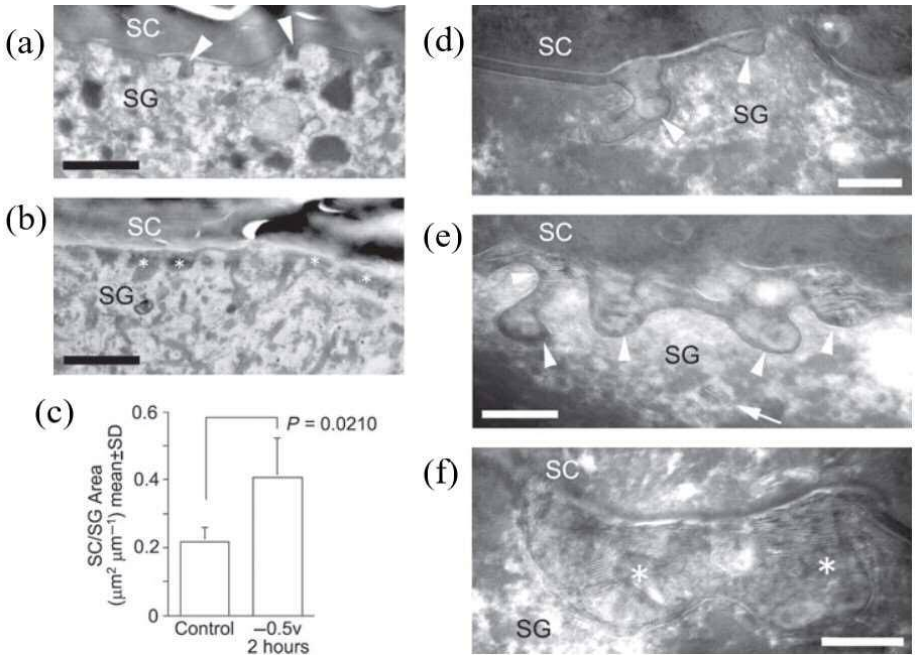

Figure 2-1.

Electron microscopic observation of lipids in human skin tissue with or without loading of negative external electric potential. (a) Osmium tetroxide postfixed control skin (Bar = 100 nm). (b) Osmium tetroxide postfixed skin after loading of external negative potential (Bar = 100 nm). In the control skin, a few sites of exocytosis were observed (a: arrowheads), while fusion of secreted lipids was observed in the treated skin (b: asterisks). (c) Quantitative results for the area of intercellular lipid domains between SC and SG. The area after loading of external negative potential was significantly larger than that of the control. (d) Ruthenium tetroxide postfixed control skin (Bar = 20 nm). (e, f) Ruthenium tetroxide postfixed skin after loading of electric potential (Bars = 20 nm). Bilayer structures were observed in secreted lipids (d: arrowheads). Secreted lipids were fused (e: arrowheads) or formed large intercellular lipid domains (f: asterisks).

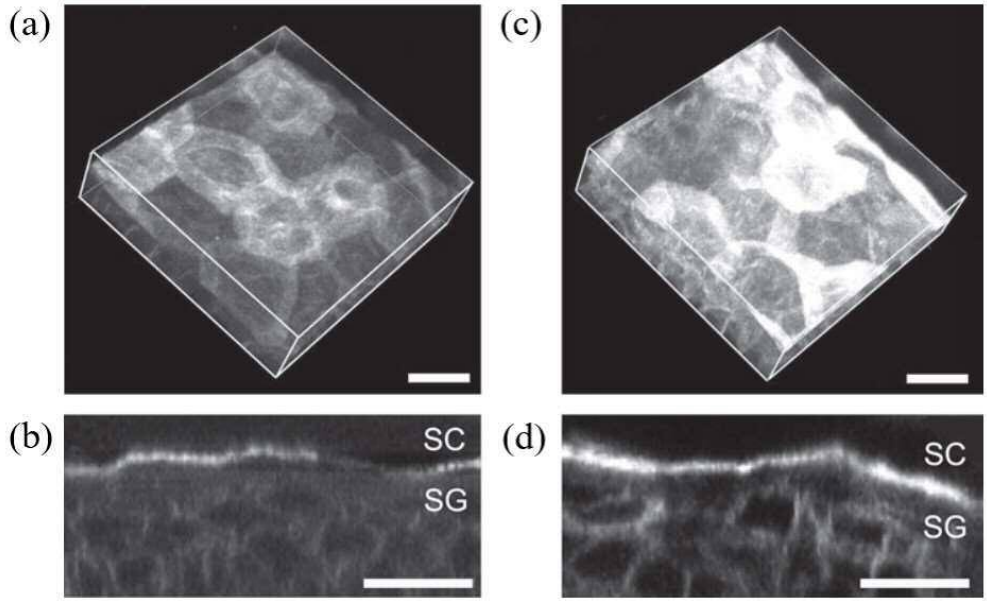

Figure 2-2.

Two-photon laser microscopic observation of intracellular calcium in human skin tissue with or without loading of negative external electric potential. (a) Three-dimensional image of control skin (Bar = 20 μm). (b) section of control skin (Bar = 20 μm). (c) Three-dimensional image of treated skin (Bar = 20 μm). (d) section of treated skin (Bar = 20 μm). The calcium gradient is larger in treated skin than in control skin.

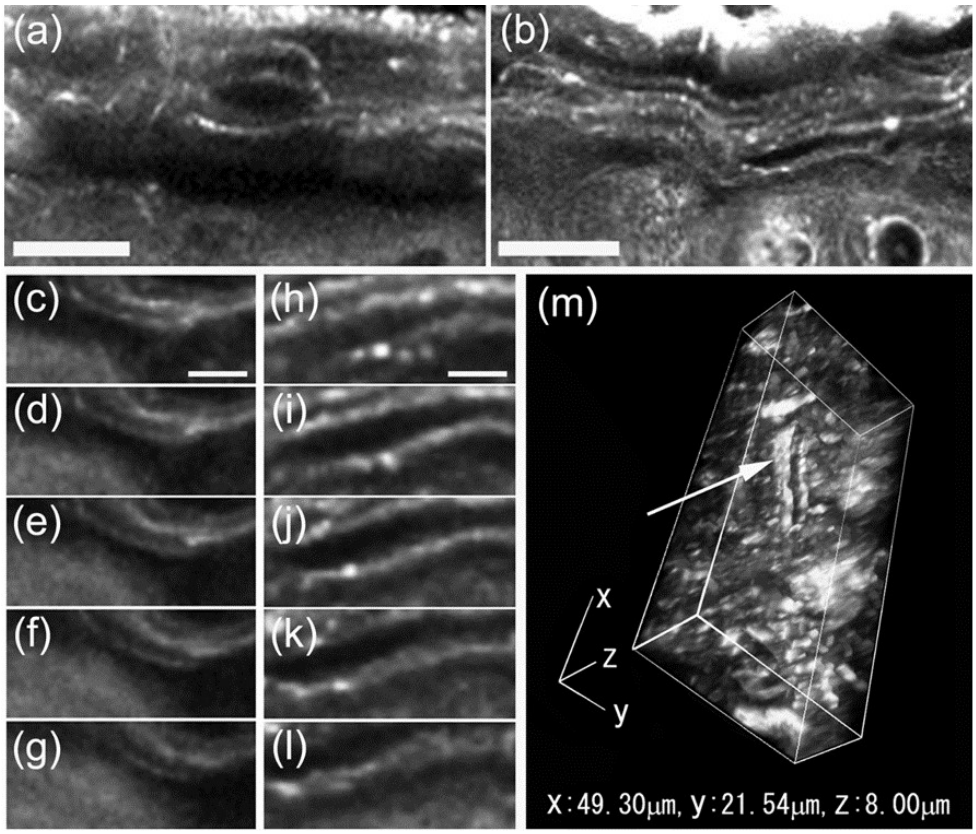

Figure 2-3.

Two-photon laser microscopic observation of lipids in human skin tissue loaded or not loaded with negative external electric potential. (a) Control skin (Bar = 10 μm), (b) Treated skin (Bar = 10 μm). (c-g) Sections of control skin at intervals of 1 μm (Bars = 2 μm). (h-l) Sections of treated skin at intervals of 1 μm (Bars = 2 μm). Longer intercellular lipid domains were observed in treated skin than in control skin. (m) Three-dimensional image of treated skin. Clear intercellular lipid domains can be seen (arrows). The length of each axis is indicated.

Chapter 3. Japanese Cedar (*Cryptomeria japonica*) pollen allergen induces elevation of intracellular calcium in human keratinocytes and impairs epidermal barrier function of human skin ex vivo

3-1. Introduction

Allergic symptoms caused by IgE-mediated type 1 hypersensitivity reaction to pollen allergens occur worldwide (16). For example, approximately 25 % of the population in Japan suffers from cedar pollinosis (20). Symptoms can cause irritation of the throat and hay fever, as well as eye and nose inflammation (85). Further, hydration of the stratum corneum is impaired in patients with seasonal allergic rhinitis (86). Mite and cockroach allergens activate PAR-2 in epidermal keratinocytes and delay epidermal permeability barrier recovery after disruption, and PAR-2 is known to be expressed in epidermal keratinocytes (23, 24). The cedar pollen allergen CPA63 exhibits protease activity that might directly activate PAR-2(87). Moreover, the airway epithelial barrier is damaged by protein extracts from several pollens (88). In addition, Denda *et al.* previously demonstrated that elevation of intracellular calcium level induced by calcium ion influx into epidermal keratinocytes delayed barrier recovery (12). Based on these findings, I hypothesized that the major cedar (*Cryptomeria japonica*) pollen allergen in Japan, Cry j1, might induce elevation of intracellular calcium in keratinocytes and impair barrier function via activation of PAR-2. Cry j1 is a basic glycoprotein with pectate lyase activity, consisting 353 amino acid residues (21, 22).

To test the above idea, I first evaluated the effect of Cry j1 on intracellular calcium level in cultured human keratinocytes. Then, I established a barrier function evaluation method using human skin tissue culture system and examined the effect of the allergen after barrier disruption. I also evaluated the protease activity of Cry j1 and culture medium of Cry j1-stimulated keratinocytes, and the effects of a trypsin inhibitor and a PAR- 2 antagonist on the actions of Cry j1.

3-2. Materials and methods

Cells and cell culture

Normal human epithelial keratinocytes were purchased from Kurabo (Osaka, Japan) and cultured in EPILIFE-KG2 (Kurabo, Osaka, Japan). Keratinocytes were seeded onto collagen-coated glass coverslips (Matsunami, Osaka, Japan) and used within 4 days. Keratinocytes were first grown to 100 % confluency in low-Ca^{2+} (0.06 mM) medium for 48 h and then incubated with high-Ca^{2+} (1.8 mM) medium for 24-48 h.

Materials

I purchased Cry j1 from Hayashibara Co., Ltd (Okayama, Japan), soybean trypsin inhibitor (SBTI) from Sigma-Aldrich (St. Louis, MO, USA), and PAR2 antagonist FSLLRY-NH2 (FSY-NH2) (89) from Tocris (Bristol, UK).

Calcium imaging of human epidermal keratinocytes

Changes of intracellular calcium concentration in single cells were measured with Fura-2 AM according to the manufacturer's instructions (Molecular Probes Inc., OR, USA). Briefly, cells were loaded with 5 μM Fura-2 AM at 37 ˚C for 45 min. After loading, the cells were rinsed with balanced salt solution containing (in mM): NaCl 150, KCl 5, $CaCl_2$ 1.8, $MgCl_2$ 1.2, HEPES 25, and D-glucose 10 (pH 7.4), abbreviated as BSS (+), and incubated for a further 10 min at room temperature to allow de-esterification of the loaded dye. The coverslip was mounted on an inverted epifluorescence microscope (ECLIPSE Ti, Nikon, Tokyo, Japan), equipped with a 75 W xenon lamp and band-pass filters of 340 and 380 nm. Imaging was done with a highsensitivity CCD camera (ORCA-R2, Hamamatsu Photonics, Hamamatsu, Japan) under the control of a Ca^{2+} analyzing system (AQUACOSMOS/RATIO, Hamamatsu Photonics).

Protease assay

For the assay of protease activity, I used two assay kits: Amplite™ Universal Fluorimetric Protease Activity Assay Kit *Green Fluorescence* (AAT Bioquest, Sunnyvale, CA, USA) and Protease Activity Fluorometric Assay Kit (BioVision, Milipitas, CA, USA). Cry j1 itself was evaluated at concentrations of 10, 100 ng/ml and 1 μg/ml in 500 μl of assay buffer. For evaluation of protease activity in culture medium, human keratinocytes were incubated with 500 μl of 100 ng/ml, 1 and 100 μg/ml Cry j1

in 10 cm dishes with gentle shaking for 1 min, or with Cry j1 in 5 ml EPILIFEKG2 for 24 h, and protein in the medium was concentrated with Amicon Ultra-0.5 ml Centrifugal Filters for Protein Purification and Concentration (Merck Millipore, Darmstadt, Germany), which gave a concentration factor of 13.1-18.1 times. Further, to examine the time course of protease activity in the medium with or without SBTI (final concentration 1 μM) or FSY-NH2 (final concentration 100 μM), I added 500 μl of the Amplite^{TM} kit substrate (fluorescent casein conjugate, diluted 1:100) to the culture of differentiated human keratinocytes, then added 10 μl of BSS (+) solution with/without Cry j1 (100 ng/ml), and imaged the fluorescence (excitation filter of 455-485 nm and emission filter of 500-545 nm) with a high-sensitivity CCD camera (ORCA-R2, Hamamatsu Photonics, Hamamatsu, Japan) under the control of a Ca^{2+} analyzing system (AQUACOSMOS/RATIO, Hamamatsu Photonics).

Human skin *ex vivo*

As describe in chapter 2, human skin tissues were purchased from Biopredic International (Rennes, France) via KAC Co., Ltd. (Kyoto, Japan). The samples had been obtained following plastic surgery, with informed consent. The excised skin was dermatomed to 340-440 μm thickness (containing epidermis and dermis), and then discs (10 mm in diameter, thickness about 2 mm) were punched out and transferred to our laboratory. Four samples of skin tissues from abdomen of healthy, independent subjects were used for the study (32, 36, 37, 39 years old, Caucasian females). This study was approved by the ethics committee of Shiseido, in accordance with the guideline of the National Institute of Health. Tissues were cultured in long-term skin culture medium (LTSC medium), provided by Biopredic International.

Transepidermal water loss

Gravimetric transepidermal water loss (TEWL) was measured as described by Hanley *et al* (90). Skin sections were placed dermis-side down onto glass-based dishes and the lateral edges and dermal surface were sealed with petrolatum, so that water loss occurred only through the epidermal surface. Before application of Cry j1 with/without other reagents, the stratum corneum was stripped 10 times with adhesive tape. Skin sections were kept at ambient temperature (37 ˚C) and humidity (30-35 %), and weighed every 2 h. TEWL levels are reported as milligrams of water lost per square millimeter per hour. Skin sections from four different subjects were used.

Electron-microscopic observation

As describe in chapter 2, Skin samples for electron microscopy minced (< 0.5 mm^3 pieces) and fixed overnight in modified Karnovsky's fixative. They were then post-fixed in 2 % aqueous osmium tetroxide or 0.2 % ruthenium tetroxide as described previously (91). After fixation, all samples were dehydrated in graded ethanol solutions, and embedded in an Epon-epoxy mixture. The area ratio of SC/SG lipid domains was quantified using osmium post-fixed material. Measurements were made without knowledge of the prior experimental treatment. These parameters were evaluated from photographs of randomly selected sections at a constant magnification, using computer software (NIH Image).

Statistics

Statistical significance of differences among three or more groups was determined by ANOVA with Fisher's protected least significant difference. $P < 0.05$ was considered significant. Student's t test was used to determine the significance of differences between the two groups.

3-3. Results

Quantitative data for intracellular calcium concentration are shown in Figure 3-1. The intracellular calcium concentration was significantly increased by 10 and 100 ng/ml Cry j1. The intracellular calcium elevation induced by 100 ng/ml Cry j1 was significantly reduced by pre-application of 1 μM SBTI or 100 μM of FSY-NH2. I observed 4 pools for each treatment. Each microscope field covered approximately 200 cells (Figure 3-1(a)).

Figure 3-1(b) shows a representative profile of the changes of intracellular calcium concentration after application of 100 ng/ml Cryj1 with or without FSY-NH2. The parameter of the vertical scale is the ratio of the emission intensity at 340 nm to that at 380 nm. When I applied Cry j1 with FSY-NH2, the fluorescence ratio showed a small, rather broad increase of 0.1 unit. When I applied the same amount of Cry j1 without FSY-NH2, a much larger, sharp increase of 0.4 unit was observed. Images obtained at 0 min (control), 2 min (peak for Cry j1 plus FSY-NH2), and 5.8 min (peak for Cry j1 alone) after the start of observation are also shown.

I next examined protease activity. Cry j1 itself showed no protease activity with the two different assay kits (data not shown). Culture medium from human keratinocytes incubated with Cry j1 for 1 min or for 24 h also showed no detectable activity (data not shown). However, when I examined the time course of protease activity in culture medium, I observed a rapid and transient increase of fluorescence of the AmpliteTM kit substrate in the presence of Cry j1, whereas the control (without Cry j1) showed a continuous gradual decrease of fluorescence due to quenching. The transient increase of the protease activity was blocked by SBTI or FSY-NH2 (Figure 3-1(c)). Quantitative comparison (n = 4) showed that the fluorescence ratio at 30 s after application of Cry j1 was significantly greater than that of the control. Inhibition of the transient increase of the activity by SBTI and/or FSY-NH2 was also statistically significant in terms of both fluorescence ratio and number of activated cells (Figure 3-1(d, e)).

The changes of TEWL in response to application of Cry j1 alone or with SBTI and FSY-NH2 are shown in Figure 3-2. Compared with the control (tape stripping + water), application of Cry j1 dramatically impaired barrier function. However, when we applied SBTI or FSY-NH2 with Cry j1, the decrease of the barrier function by Cry j1 was almost completely blocked. Electron-microscopic observations supported the results of the barrier study. Application of Cry j1 prevented lamellar body secretion, as compared with the tape-stripped control, while co-application of trypsin inhibitor and PAR-2

antagonist with Cry j1 normalized the lamellar body secretion (Figure 3-3).

3-4. Discussion

The changes of intracellular calcium concentration measured in vitro suggested that the PAR-2 receptor was activated by Cry j1, leading to elevation of intracellular calcium. Activation of PAR-2 requires protease activity, and although Cry j1 itself showed no detectable activity, I observed a rapid (within 30 s) and transient increase of protease activity in the medium after addition of Cry j1 to the cultured keratinocytes. Assays of protease activity in the medium with two commercial kits had failed to detect this increase, because of insufficient time resolution (it took at least 4 min to measure the activity). Denda *et al.* previously demonstrated that trypsin-type protease activity increases in the epidermis immediately after barrier disruption of human skin (80). Thus, I speculate that a trypsin-type protease might have been induced immediately upon contact of Cry j1 with keratinocytes and then rapidly autolyzed or inactivated. This seems plausible, because if the protease remained active, barrier recovery might be extremely slow, and serious inflammation might be induced. Many endogenous serine proteases are expressed in skin (92). I speculate that epidermal keratinocytes contain an endogenous factor(s) that regulates protease activity.

The *ex vivo* studies supported the idea that Cry j1 impaired epidermal barrier homeostasis by inducing activation of PAR-2. Denda *et al.* previously demonstrated that influx of calcium into keratinocytes at the uppermost layer of the epidermis after barrier disruption prevented the lamellar body secretion, resulting in delayed barrier recovery (12). In the present study, electron-microscopic observation confirmed that Cry j1 blocked lamellar body secretion.

An interesting possibility is that the impairment of epidermal barrier function by Cry j1 might promote entry of Cry j1 and/or other allergens into the skin, exacerbating allergic reaction. Moreover, PAR-2 activation sensitizes TRPV1 and TRPA1, which are well-known pain and itching receptors (93-95). Thus, Cry j1 might directly induce itching or pain, which is a common feature of skin allergic reaction. These results suggest that topical application of trypsin-type protease inhibitor or PAR-2 inhibitor might clinically effective for the treatment of Cry j1-induced allergy.

3-5. Figures

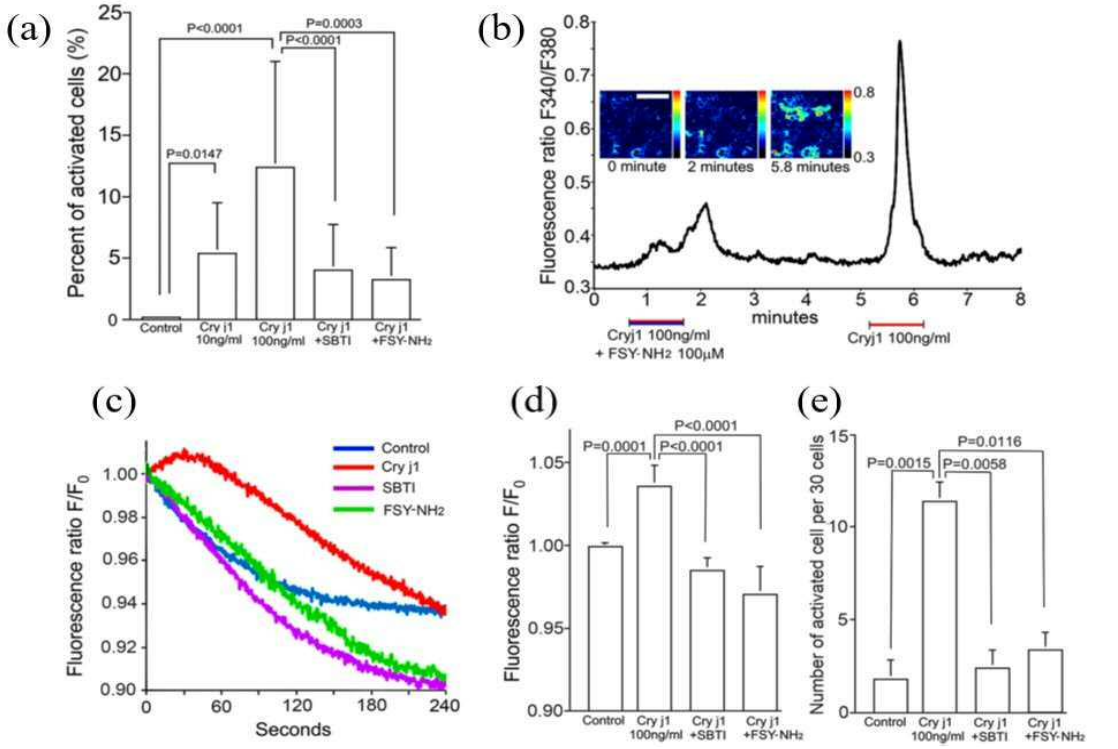

Figure 3-1.

Effects of Cry j1 on cultured human keratinocytes. (a) Quantitative determination of percentage of activated cells after application of Cry j1 with or without SBTI and FSY-NH2. The intracellular calcium elevation induced by 100 ng/ml Cry J1 was significantly reduced by pre-application of 1 μM SBTI or 100 μM FSY-NH2. Bars and lines represent mean + SD. (b) Changes of intracellular calcium (expressed as the ratio of fluorescence intensities at 340 and 380 nm). Application of 100 ng/ml Cry j1 with 100 μM FSY-NH2 increased the level of intracellular calcium by approximately 0.1 unit, while the same amount of Cry j1 without FSY-NH2 increased the level of intracellular calcium increased by approximately 0.4 units. Images obtained at 0 (control), 2 min (peak for Cry j1 plus FSY-NH2), and 5.8 min (peak for Cry j1 alone) after the start of observation are also shown. Bar = 200 μm. (c) Time course of protease activity (expressed as fluorescence ratio of AmpliteTM kit substrate). Application of Cry j1 to cultured human keratinocytes at time 0 s induced a rapid, transient increase of protease activity (red line). After application of BSS (+) only (control), the fluorescence level

gradually decreased (blue line). The transient increase of protease activity was blocked by SBTI (purple line) or FSY-NH2 (green line). Vertical scale is normalized by the fluorescence at time 0. Note vertical scale is different from (b). (d) Quantitation of fluorescence change at 30 s after application (n = 4). A significant difference was observed between the control and Cry j1 application groups. SBTI and FSY-NH2 each significantly blocked the increase. e Numbers of activated cells per 30 cells showed similar differences to (d) (n = 3-5). Bars and lines represent mean + SD.

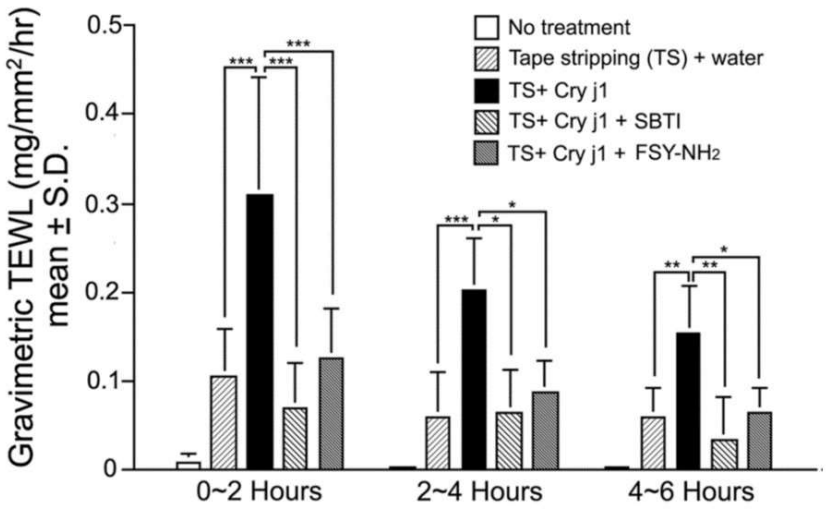

Figure 3-2.

Ex vivo evaluation of water-impermeable barrier function after application of Cry j1 with or without SBTI and FSY-NH2. The vertical axis shows the amount of water loss during 0-2, 2-4 or 4-6 h after TS. Application of Cry j1 dramatically increased the water loss. The Cry j1-induced increase was significantly reduced by coapplication of SBTI or FSY-NH2.

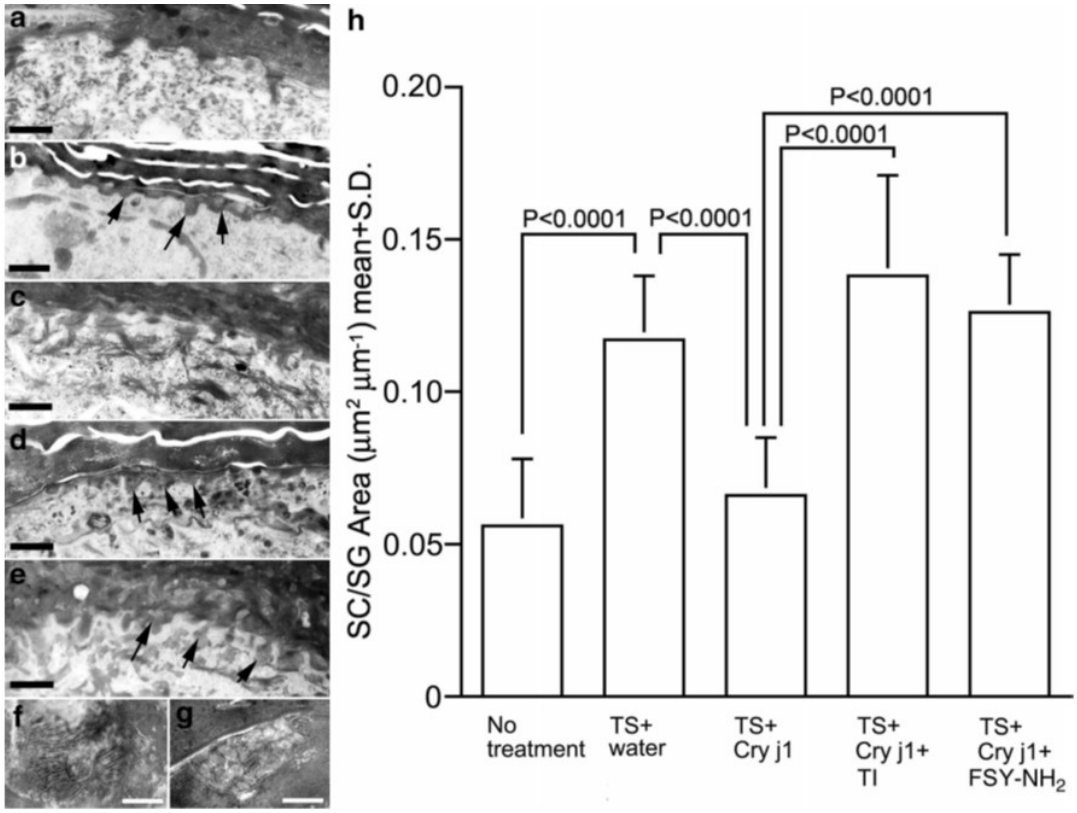

Figure 3-3.

Electron-microscopic observation of *ex vivo* skin samples. (a) No treatment. (b) Tape stripping (TS) 10 times and application of water. (c) TS and application of 100 ng/ml Cry j1. (d) TS and application of 100 ng/ml Cry j1 and 1 μM SBTI. (e) TS and application of 100 ng/ml Cry j1 and 100 μM FSY-NH2. Arrows indicate secreted lipids between SC and SG. Bars = 1 μm. (f) Magnified image of secreted lipids after TS and application of water. (g) Magnified image of secreted lipids after TS and application of Cry j1 and FSY-NH2. Bars = 100 nm. (h) Quantitative evaluation of the area ratio of SC/SG lipid domains. A significant increase of the intercellular lipid domain was observed after tape stripping and it was reduced by application of Cry j1. The effect of Cry j1 was blocked by co-application with SBTI or FSY-NH2.

Chapter 4. Real-time imaging of human epidermal calcium dynamics in response to point laser stimulation

4-1. Introduction

Calcium ions are involved in epidermal barrier homeostasis and keratinocyte differentiation (96, 97), as well as in various aspects of epidermal physiology, including keratinocyte proliferation (98). Moreover, intracellular calcium dynamics is thought to play an important role in skin sensation. Denda and Tsutsumi *et al.* previously reported the dynamics of intracellular calcium in cultured keratinocytes in response to air exposure and mechanical stimulation (45, 99). It is well established that epidermal keratinocytes express multiple sensory receptors that are also found in peripheral nerve fibers (34, 36), and Denda *et al.* have suggested that keratinocytes might function as a skin sensory system (76). For example, activation of the receptor TRPV1 in keratinocytes induced nociception (100). As regards the signaling mechanism, keratinocytes contain ATP receptors (101) and stimulation of keratinocytes results in release of ATP, which in turn induces elevation of intracellular calcium (44, 45). In addition, intercellular communication might occur in epidermis via gap junctions; for example, some connexin family members have been found in keratinocytes, and gap-junction blockers suppressed calcium propagation in response to mechanical force or air exposure (99, 102, 103). Thus, it is plausible that calcium dynamics in human skin has a central role in mediating responses to external stimuli. The aim of this study was to demonstrate a novel method for real-time measurement of calcium dynamics in response to point stimulation of *ex vivo* human epidermis and cultured keratinocytes in the presence of an intracellular calcium indicator. Using the emission laser of a two-photon microscope for point stimulation of cells in SG, I was able to observe real-time calcium propagation throughout thick (30-100 mm) cross-sections of living epidermis by means of two-photon microscopy. These methods should be valuable for studies of epidermal physiological responses to various external stimulations, at the single-cell level.

4-2. Materials and methods

Human skin *ex vivo*

As describe in chapter 2, Human skin tissues were purchased from Biopredic International (Rennes, France) via KAC Co., Ltd. (Kyoto, Japan). The tissues had been collected during plastic surgery after informed consent had been obtained. The donors were 8 healthy, independent Caucasian women, aged 31-44 years. The excised skin was full-thickness skin (containing epidermis, dermis and fat layer), punched into discs (12 or 16 mm in diameter). This study was approved by the ethics committee of Shiseido, in accordance with the guidelines of the National Institute of Health. Tissues were put on sterilized filter papers and cultured at 37 ˚C in long-term skin culture medium (LTSC medium), provided by Biopredic International. During tissue culture, SC of the tissue was kept dry (not immersed in the medium).

Two-photon laser stimulation and observation of intracellular calcium propagation

The fat layer was removed from the samples, and 6 mm diameter discs were punched out. Each disc was cut in half, and loaded with 10 μM OG and 10 μM Cell Tracker™ Red CMTPX (CTR, Molecular Probes Inc., OR, USA) at 37 ˚C for 2 h in LTSC medium. Only a cross-section of the sample was immersed in the loading solution. After loading, the samples were rinsed with balanced salt solution (BSS) containing (in mM): NaCl (150), KCl (5), $CaCl_2$ (1.8), $MgCl_2$ (1.2), HEPES (25), and D-glucose (10) (pH 7.4) at room temperature, and placed on a glass-bottomed dish (Matsunami, Osaka, Japan) with the cross-section of the tissue facing the glass. The tissue was observed under a two-photon laser-scanning inverted microscope (A1R MP, Nikon, Tokyo, Japan) equipped with a pulsed femtosecond Ti-sapphire laser (Mai Tai Deep See, Spectra Physics, CA, USA). The excitation laser wavelength was 810 nm, and 500-550 nm (for OG) and 601-657 nm (for CTR) band pass filters were used for emission. A 40X water immersion objective lens was used. All two-photon images were constructed using NIS-Elements software (Nikon). Laser stimulation of the uppermost part of the stratum granulosum was performed with the pulsed laser (wavelength was 810 nm) on the microscope (maximum power for 1 s; controlled by the NIS Elements software). First, the fluorescence intensity of the unstimulated tissue was measured for 20 s, then point stimulation was conducted with the laser (1 s), and the fluorescence intensity was measured for 1 min. During the experiments, fluorescence intensity was measured every 1 s. Apyrase and 1-octanol were purchased from Sigma-Aldrich (St. Louis, Mo., USA).

Carbenoxolone disodium was purchased from LKT Laboratories (St. Paul, MN, USA). Apyrase was applied at the concentration of 100 U/ml, octanol at 50 mM, and carbenoxolone at 100 μM in BSS. The tissues were pre-incubated in BSS and the solution was changed to one containing apyrase or octanol or carbenoxolone; stimulation and observation were carried out within 30 min after changing the solution.

Changes of fluorescence intensity in cells within a circle of radius 75 μm centered on the stimulation point were measured. Each reagent was tested using tissues from 4 donors. Data analysis was performed using Microsoft Excel and Kaleida Graph (Synergy Software, PA, USA). I calculated the average (F_0) and SD (σ) of fluorescence intensities before stimulation. Maximum intensity for 1 min after stimulation was defined as F_{max}. I defined cells that met the following criterion as activated cells: (F_{max} - F_0) $\geq 5\sigma$. One-way analysis of variance (ANOVA) and Tukey's test were used to examine the significance of differences between groups.

Calcium imaging of human epidermal keratinocytes

As describe in chapter 3, Normal human epithelial keratinocytes were purchased from Kurabo (Osaka, Japan) and cultured in EPILIFE-KG2 (Kurabo). Keratinocytes were seeded onto glass-bottomed dishes (Matsunami) coated with collagen type-IV (Sigma). Keratinocytes were grown to 100% confluency in low-Ca^{2+} (0.06 mM) medium. Cells were loaded with 5 μM OG at 37 ˚C for 45 min in culture medium, and then rinsed with BSS. Observation and laser stimulation of the cells were performed as described in the case of skin tissues. Laser stimulation was performed in BSS within 30 min after application of 10 U/ml apyrase, or in the absence of apyrase, and the fluorescence intensities of all cells in the observation area surrounding the stimulation site were measured. ANOVA was used to determine the significance of differences between with and without apyrase.

Calcium imaging of ATP-perfused skin slices

Human skin tissues were immersed in cutting solution containing (mM) NaCl (136), KCl (5), NaH_2PO_4 (1.25), $NaHCO_3$ (22), glucose (30), sucrose (170), $CaCl_2$ (1.8), and $MgCl_2$ (1), and mounted in 10 % agarose gel. Vertical, 300 μm thick slices of the mounted skin were cut with a vibratome (VT1200 S, Leica Microsystems). The slices were incubated in cutting solution containing 10 μM fura-2, AM (Molecular Probes) for 2 h at room temperature, and imaging was carried out with an inverted fluorescence microscope (ECLIPSE Ti, Nikon), equipped with a 75 W xenon lamp, excitation filters of 340 (327 - 353) nm and 380 (381 - 392) nm, and an emission filter of 468 - 552 nm.

Images were observed using a 10X objective lens and captured with a digital CCD camera (ORCA-R2, Hamamatsu Photonics, Hamamatsu, Japan). Changes of intracellular calcium were evaluated with a calcium analyzing system AQUACOSMOS/ RATIO (Hamamatsu Photonics), and results are presented as the ratio of fluorescence intensities with excitation at 340 and 380 nm. Perfusion of 100 μM ATP solution was performed for 4 min and then ATP was washed out using a perfusion valve controller (VC-6, Warner Instruments, CT, USA).

4-3. Results

Figure 4-1 shows three-dimensional images of human epidermis labeled with OG and CTR. All living epidermal cells were clearly labeled with CTR and resolution was at the single-cell level. The OG fluorescence, a measure of intracellular calcium level, was most intense in SG, and was also intense in SB. Some cells showed very high intensity through the 500-550 nm emission filter (for OG) and low intensity through the 601-657 nm filter (for CTR). I considered that these cells were dead or dying, because CTR is a fluorescent dye that is retained in living cells and is used for monitoring cell location. Indeed, many cells at the sectioned surface showed similar characteristics, so the sectioning process might have damaged them. However, with the two-photon microscope, we could observe internal regions of the skin far from the sectioned surface.

Figure 4-2 shows time-course fluorescence images of OG-loaded human epidermis or cultured keratinocytes before and after laser stimulation. Immediately after the stimulation, elevation of intracellular calcium was observed in cells located just below the stimulation site (Figure 4-2(a), 23 s; red arrow indicates stimulation site and yellow arrows indicate cells in which elevation of intracellular calcium has started). Calcium propagation after stimulation varied in each layer of epidermis (36 - 80 s; yellow arrows indicate cells in which elevation of intracellular calcium has started, as in the picture at 23 s). Figure 4-2(b) shows the profiles of fluorescence change in individual cells. Cells adjacent to the stimulation site were activated immediately after the stimulation, but the elevation of intracellular calcium was relatively small (cell numbers 2, 3 in Figure 4-2b). Elevation of intracellular calcium in cells of the stratum basale was higher than that of cells in the uppermost layer. In stratum basale, I observed clear intercellular calcium propagation to cells far from the site of stimulation (cell numbers 10, 11). I also examined stimulation of the SC, but in this case no elevation of intracellular calcium was observed (data not shown). These results indicate that laser stimulation of living cells in epidermis induced calcium propagation, and that heat loading due to laser stimulation of SC did not affect the calcium responses. In cultured keratinocytes, calcium propagation began close to the stimulation site (Figure 4-2(c, d)). The elevation of intracellular calcium tended to be greater in cells closer to the center of the stimulation site. Next, I applied ATP to human skin slices and observed the dynamics of intracellular calcium (Figure 4-3). The elevation of calcium in cells after ATP application was greater in cells in lower epidermal layers among all 3 donors examined.

Figure 4-4(a) shows the percentage of activated cells in human skin epidermis during 1 min after laser stimulation in the presence of apyrase or gap-junction blocker (octanol or carbenoxolone). Cellular activation was significantly reduced in the presence of apyrase. Both gap-junction blockers inhibited calcium propagation. Co-application of apyrase and gap-junction blocker potently blocked calcium propagation. Figure 4-4(b) shows the results for cultured keratinocytes; activated cells were reduced to < 10% in the presence of apyrase. Figure 4-4(c, d) shows images of activated cells in epidermis and cultured keratinocytes after laser stimulation. Yellow arrows indicated the basal layer of the epidermis and red arrowheads indicated stimulated areas. Application of apyrase or gap-junction blocker decreased calcium propagation.

4-4. Discussion

The calcium gradient in human epidermis is altered by epidermal barrier disruption (2, 104), as well as in aged skin and some skin diseases (2, 105, 106). Menon and Elias demonstrated that intracellular calcium is increased in the upper layer of SG of psoriatic skin in comparison with healthy skin (105), and Bosen *et al.* showed that the epidermal calcium gradient was altered in a keratitis-ichthyosis-deafness model mouse, while ceramides, which are major components of extracellular lipids in SC, were markedly decreased (106). Further, Kobayashi *et al.* developed a mathematical model that highlights the key role of calcium gradation in epidermis barrier homeostasis (58). In the present study, I confirmed that the intracellular calcium concentration in SG was highest, while that in stratum basale was also high, in agreement with a previous report (107). Then, I employed two-photon microscopy to observe calcium dynamics at the single-cell level after point stimulation with a laser, using cultured keratinocytes and thick sections of human skin tissue.

In cultured keratinocytes, calcium propagation showed a concentric wave pattern, and the increase of intracellular calcium was greater in cells closer to the stimulation site. In culture, all keratinocytes have similar properties, whereas in epidermis, keratinocytes differentiate as they pass from SB to SC, and the expression levels of receptors and channels change. Indeed, these observations of cross-sections of living epidermis showed that elevation of calcium in response to stimulation of the uppermost layer of SG was highest in SB, which is the furthest stratum from the stimulation site. Proksch *et al.* demonstrated that after cutaneous barrier disruption with acetone, an increase of DNA synthesis occurred only in the epidermal basal layer, and they suggested that the cutaneous barrier regulates epidermal DNA synthesis (108). Another report showed that exposure to low humidity increased epidermal DNA synthesis, and when the barrier was disrupted under low humidity condition, DNA synthesis was increased only in SB; further, the epidermis was thicker than under a higher humidity condition (109). Thus, it is plausible that the calcium response at the SB might be a trigger of epidermal DNA synthesis after stimulation.

Koizumi *et al.* reported that signal transduction from keratinocytes to neurons is mediated by ATP released from mechanically stimulated keratinocytes (44). Tsutsumi *et al.* previously reported that the increase of intracellular calcium in response to ATP varied in each layer of epidermis, and was greater in SB than in the uppermost layer of rat skin slices (110). Here, I also perfused human skin slices with ATP (Figure 4-3), and

observed that the elevation of calcium of cells after ATP application was greater in cells in the lower epidermal layers. Calcium propagation was inhibited in the presence of apyrase, indicating the involvement of ATP released from damaged cells and adjacent cells. Cells in the basal layer appear to be more sensitive to ATP than other cells in epidermis. Inoue *et al.* reported that the expression of purinergic receptor family members is influenced by keratinocyte differentiation (43). It has also been suggested that ion pumps in keratinocytes might contribute to the electrophysiological status of the epidermis, and ion movement in epidermis might contribute to skin homeostasis (4). Keratinocytes contain various calcium channels and some of them are expressed heterogeneously in epidermis (76, 111). Therefore, different responses of keratinocytes in different epidermal layers might be caused by differences in expression or distribution of receptors or ion channels.

ATP also plays an important role as a second messenger via gap junctions in epidermis. Connexin gap-junction proteins are expressed in epidermis, and can be blocked by octanol or carbenoxolone (102, 103, 112). Further, pannexin 1, which is also blocked by carbenoxolone (103, 113), is expressed in wounded epidermis and is activated by ATP through purinergic P2Y receptors and by intracellular calcium (114, 115). Octanol and carbenoxolone also block P2X7 receptors in spinal cord astrocytes (116). Thus, when the uppermost layer of the epidermis is subjected to external stress, many receptors and channels in keratinocytes would be activated via ATP and other transmitters, intracellular calcium would be elevated, and finally a signal might be transmitted to nerve endings.

It is noteworthy that cells in SB and directly under the stimulation site in the present work responded very quickly to laser stimulation, and this would be consistent with a role in skin perception. A previous study demonstrated that keratinocyte receptor TRPV1 mediates a physiological nociceptive response in mice (100), which is consistent with the idea that the responses of keratinocytes to external stimulation might be rapidly transferred to nerve fibers via intercellular propagation of calcium concentration changes among keratinocytes.

Although cell activation was highest in SB, we also observed calcium propagation in other layers (Figure 4-2(a, b)). Calcium elevation in SS was smaller than that in SB, but interestingly, it was less efficiently suppressed by apyrase and gap-junction blockers. Thus, the mechanisms of calcium propagation in cells of SS might differ from those in SB. Also, intracellular calcium elevation in SS tended to persist longer than in SB (Figure 4-2(b), line 2-6). It is possible that keratinocytes in the different layers might have distinct roles in perception of various stimuli. A previous study indicated that

different types of nerve fibers were present in different layers of the epidermis (117). Thus, different types of skin sensory information from keratinocytes in each layer might be processed through these topographically distinct nerve fibers.

Keratinocytes functionally express many receptors, including modulators of intracellular calcium levels, and some receptors show differential expression in each layer of epidermis (76). These results seem consistent with our present finding that calcium responses are distinct in different epidermal layers. Examination of the interaction between keratinocyte receptors and neurons may throw new light on mechanisms of abnormal skin perception, and My method is expected to be a versatile tool for investigations of the mechanisms of physiological events in living epidermis at the single-cell level.

4-5. Figures

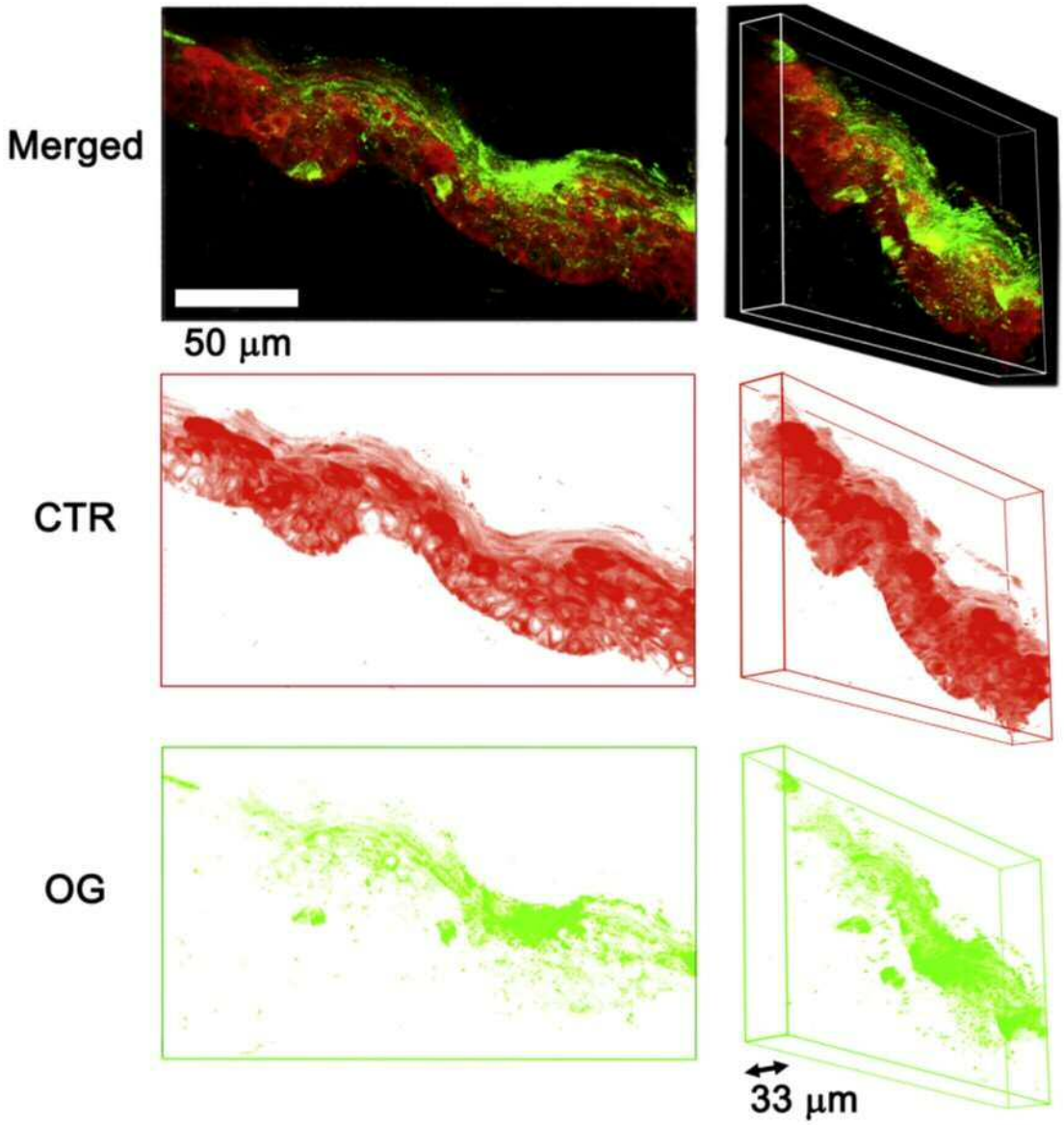

Figure 4-1.

Three-dimensional images of human epidermis labeled with Oregon Green (OG) and Cell Tracker™ Red (CTR), obtained by two-photon microscopy. Upper images are merged images, middle: CTR, and bottom: OG. Bar = 50 μm.

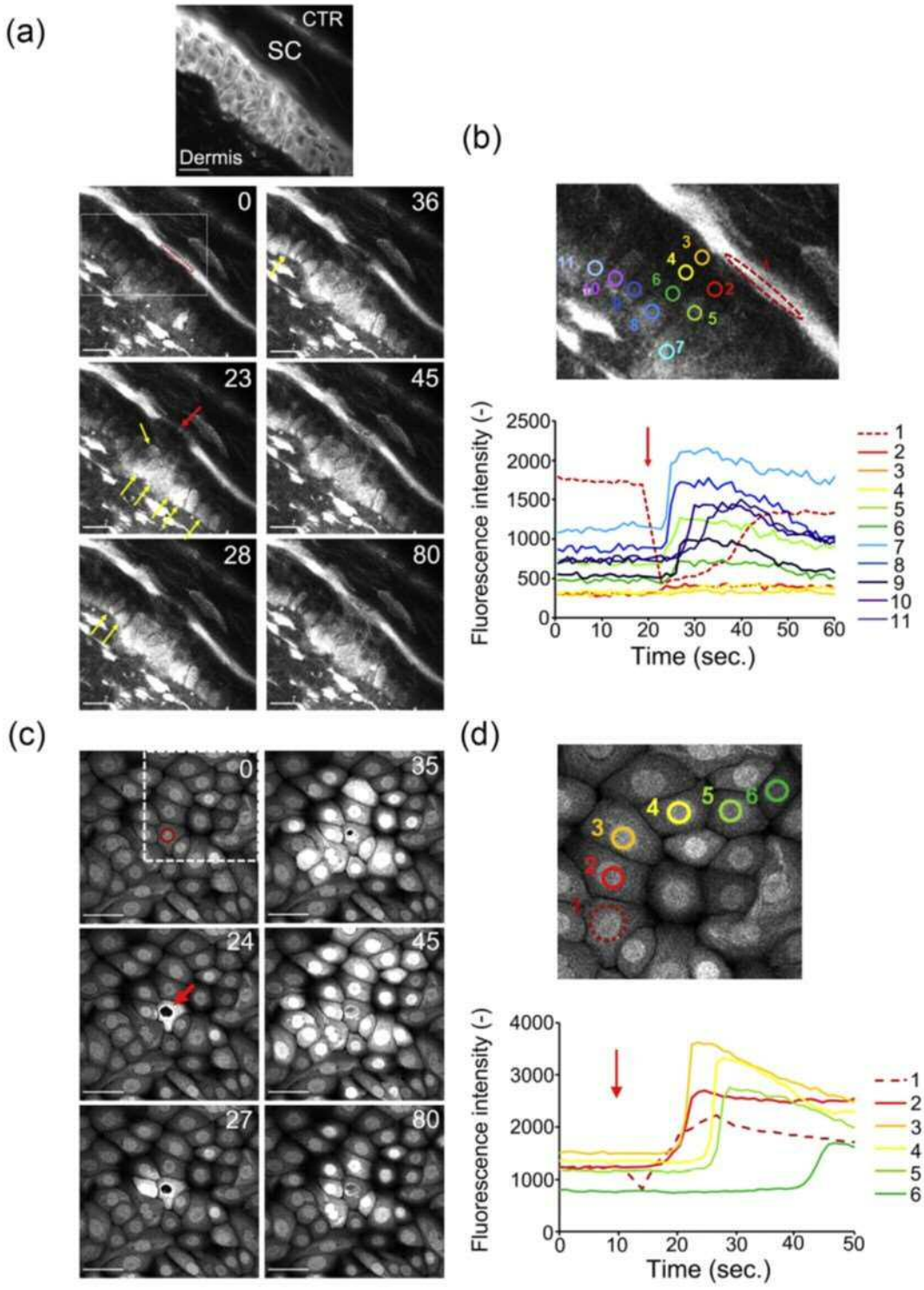

Figure 4-2.

(a, c) Fluorescence images showing the time course of calcium propagation: before stimulation (0 s) and after stimulation ((a) human epidermis, (c) proliferating keratinocytes). The upper image of (a) is a CTR-labeled image of the same location. Red ellipses in the 0 s image in (a) and (c) show the laser stimulation area. Red arrows in subsequent images show the stimulation area and yellow arrows show cells in which intracellular calcium elevation has started. Bars represent 20 μm (a) and 50 μm (c), respectively. (b, d) Profiles of calcium propagation in cells in epidermis (b) and in proliferating keratinocytes (d). Images in (b) and (d) correspond to the white dashed-line square in (a) and (c), and colored circles and numbers on the fluorescence image correspond to those on the graph. Profile 1 in (b) and (d) (red dashed line) shows the intensity at the stimulated areas. Red arrows in graphs indicate the time of stimulation.

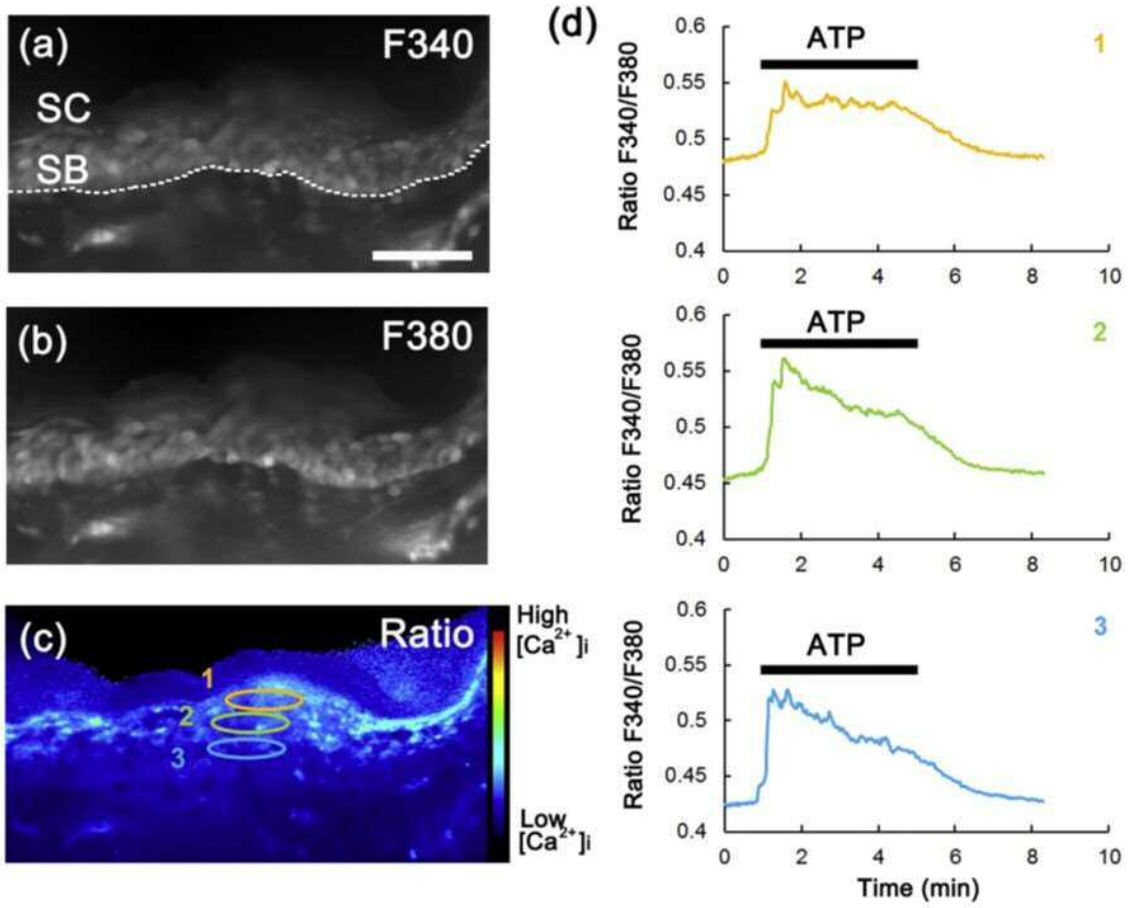

Figure 4-3.

Results of calcium imaging of a skin slice during perfusion with ATP. (a, b) Fluorescence images at excitation wavelengths of 340 nm (a) and 380 nm (b). The dashed line in (a) shows the bottom of the epidermis. (c) Pseudo-color image representing the intensity ratio (340 to 380 nm). Bars = 100 μm. (d) Profiles of intensity ratio in each layer before and after application of ATP (area 1: uppermost layer, area 2: middle layer, and area 3: bottom layer, as shown in (c)).

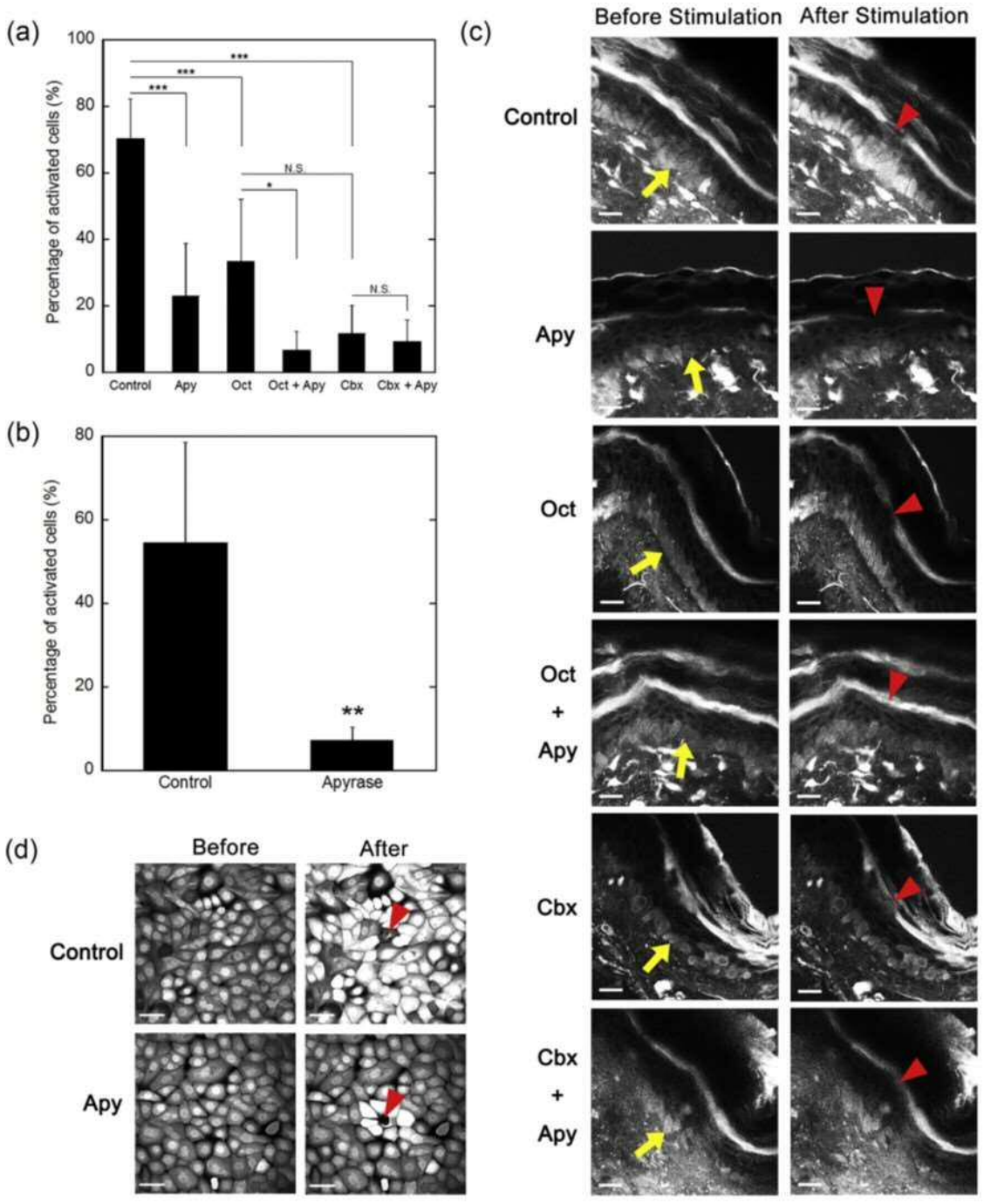

Figure 4-4.

(a) Percentage of cells activated in stratum basale after laser stimulation in the presence of apyrase (Apy), octanol (Oct), or carbenoxolone (Cbx). (b) Percentage of cultured keratinocytes activated after laser stimulation. *** $p < 0.001$, ** $p < 0.01$, * $p < 0.05$. (c, d) Fluorescence images of epidermis (c) and cultured keratinocytes (d) before and after stimulation. Yellow arrows (c) indicate basal layer of the epidermis and red arrowheads (c, d) indicated the stimulated areas. Bars represent 20 μm (c) and 50 μm (d).

Chapter 5. Mathematical-model-guided development of full-thickness epidermal equivalent

5-1. Introduction

Experimental models of human epidermis are useful research tools for basic studies of skin biology and functional mechanisms, as well as for the development of transdermally administrable medicines and safety testing of cosmetics and other products (118). However, epidermis has a complex structure consisting of multiple layers (119) and is not adequately mimicked by many current models (118). For example, epidermal models prepared with passaged keratinocytes are usually non-physiologically thin (10-20 μm), although thick epidermal equivalents (around 100 μm) have been constructed with primary keratinocytes (120). However, it is difficult to obtain primary keratinocytes with consistent properties in large amounts.

Nagayama *et al.* have established methodology for simulating epidermal homeostasis (58-60), employing a mathematical model composed of keratinocytes generated from stem cells distributed in the basal layer, and taking into account dynamic cellular processes in the epidermis, such as migration and differentiation, as well as the interaction of intracellular Ca^{2+} dynamics with differentiation. Their previous numerical simulations successfully reproduced a spatially and temporally stable epidermal structure with sufficient thickness and a flat SC/suprabasal layer interface (60). Calculations suggested that the epidermal structure and thickness are greatly influenced by the spatial distribution of stem cells and the structure of the basement membrane on which they are seeded. When they applied sinusoidal modulation of the basement membrane shape and systematically changed the amplitude and wavelength, they found that formation of a thick and stable epidermal structure required basement membrane undulations with large amplitude and short wavelength (60). This result indicated that the undulatory pattern of the papillary layer, which lies at the top of the dermis immediately below the epidermis, is critical for constructing an epidermal model with physiological thickness. However, one of the most important roles of the epidermis is its water-impermeable barrier function, which requires a sufficiently thick SC. Since their previous model (60) did not take into account flattening of corneocytes, it could not

properly simulate the thickness of SC. Here, we first established a new three-dimensional numerical simulation model that incorporates flattening of corneocytes to form a SC sheet. Then, based on the computational predictions of the improved simulation model, I examined whether a full-thickness three-dimensional epidermal-equivalent model that included SC and intercellular lamellar lipid structure, which are essential for skin barrier function, could be obtained by seeding passaged human keratinocytes on an undulating surface consisting of polyester textile with an appropriate fiber pattern in culture dishes exposed to air. These results represent a proof-of-principle of the value of this methodology for establishing high-quality epidermal-equivalent models with passaged keratinocytes, and also indicate the importance of substrate structure for epidermal development. They also support the idea that mathematical modeling of complex biological processes can have predictive ability and practical value.

5-2. Materials and methods

Mathematical model and computer simulation

The mathematical model and computer simulation methodology are described in the supplement 5-1.

Cells and cell culture

The basic methodology for constructing the skin equivalent model was as described previously (120). NHEKs from Kurabo (Osaka, Japan) were cultured in Epilife-KG2 (Kurabo) containing 0.06 mM Ca^{2+} in 10 cm dishes and passaged three times. Then, 2.2 x 10^5 keratinocytes/500 µl CnT Prime medium (CELLnTEC, Berne, Switzerland) were plated on 12-well Millicells with 0.4 µm pore size PET hanging inserts (bore diameter 12 mm, Millipore, Billerica, MA). The inserts were precoated with CellStart (Invitrogen Life Technologies, Carlsbad, CA) in a 50X dilution of DPBS. CnT Prime (CELLnTEC, Bern, Switzerland) (1 ml) was added to each well. At 72 hours after seeding (day 3) the medium was switched to CnT-PR-3D differentiation medium (CELLnTEC, Bern, Switzerland) both inside and outside the inserts. Cultures were submerged in differentiation media for 16 hours and then lifted to the air-medium interface by removing excess medium from the insert and reducing the volume of differentiation media on the outside to 500 µl. Cultures were fed daily with 500 µl of differentiation media for 9 days and then harvested. To evaluate proliferative cells, BrdU was applied in the medium 24 hours before the harvest.

Polyester textile substrates

Polyester textile (12-mm diameter; Clever, Toyohashi, Japan) with a variety of fiber patterns was fixed with Rocktite 3554 (Henkel, Düsseldorf, Germany) and RTV118 (Momentive, New York, USA) to the bottom of the inserts, then pre-coated with CellStart, and seeded with keratinocytes. Incubation was conducted as above. The characteristics of the textiles used are summarized in Table 1.

Evaluation of fiber patterns in textiles and human skin *ex vivo*

Fiber patterns of textiles and normal human skin tissues were evaluated as illustrated in Supplement Figure 5-1. As describe in chapter 2, Human tissues (non-sunexposed area from abdomen, n = 13; average age of subjects 36.3 years), obtained with informed consent following plastic surgery, were purchased from Biopredic International (Rennes,

France) via KAC Co., Ltd. (Kyoto, Japan). This study was approved by the ethics committee of Shiseido, and was conducted in accordance with the guideline of the National Institute of Health.

Yes-associated protein (YAP) siRNA application

One day before seeding cells onto 12-well Millicells, the cells were grown to 80% confluency (approximately 2-3 × 10^6 cells), and transfected with 20 nM scramble control or YAP siRNA (GE Dharmacon, Lafayette, CO, USA) using the transfection reagent RNA iMAX (Thermo Fisher Scientific, Waltham, MA USA) in OptiMem (Thermo Fisher Scientific) as described in the manual. Scramble control: ugguuuacaugucgacuaa, ugguuuacauguuguguga, ugguuuacauguuuucuga and ugguuuacauguuuuccua. YAP: gcaccuaucacucucgaga, ugagaacaaugacgaccaa, ggucagagauacuucuuaa, ccaccaagcuagauaaaga (GE Dharmacon, Lafayette, USA). Total RNA from human keratinocytes was isolated using and RNeasy mini kit (QIAGEN, Hilden, Germany) for quantitative real-time PCR (RT-PCR). Complementary DNA (cDNA) synthesis from 1 μg of total RNA was performed using SuperScript VILO Master Mix (Invitrogen, Carlsbad, USA). The PCR reactions were performed using LightCycler 480 Probes Master (Roche, Basal, Switzerland), cDNA and specific primer pairs: GAPDH: forward, gaaggtgaaggtcggagtc and reverse, gaagattggtgatgggatttc; YAP: forward, cccagatgaacgtcacagc and reverse, ttcccatccatcaggaagag, on an LightCycler 480 System II (Roche, Basel, Switzerland). Results were normalized with the GAPDH gene and showed that YAP siRNA decreased YAP expression by 87 ± 2%.

Histology

For hematoxylin and eosin (H&E) staining, anti-bromodeoxyuridine (BrdU) antibody or anti-Yes-associated protein (YAP) antibody staining, samples were fixed with 4% paraformaldehyde in PBS, embedded in paraffin, and sectioned at 3 μm. For the evaluation of areas of stratum corneum and living layer of the epidermis, we constructed 4-6 samples sections per textile. I acquired 3 images per one section and took the average value, and we used 3-5 sections from each condition. Image-J software was used to remove fiber cross-section areas from the images of the H&E-stained sections, and to evaluate the remaining area of the living layer of the epidermis, and area of stratum corneum. For immunostaining of filaggrin, loricrin, and melanoma-associated chondroitin sulfate proteoglycan (MCSP), samples were fixed in acetone at -20 °C for 30 min, embedded in paraffin and sectioned at 3 μm for staining. For tight junction markers, 6 μm frozen sections were fixed in methanol at -20 °C for 30 min. Primary

antibodies were rabbit polyclonal anti-filaggrin (1/300, # sc-30229, Santa Cruz, Dallas, USA), rabbit polyclonal loricrin (1/500, # PRB-145P, Biolegend, San Diego, USA), mouse monoclonal-anti-NG2/MCSP (1/400, # MAB2585, R&D Systems, Minneapolis, USA), rabbit polyclonal anti-claudin-1 antibody (1/500, #51–9000, Invitrogen, Carlsbad, USA) and mouse monoclonal anti-ZO-1/TJP1 antibody (1/500, #33–9100, Invitrogen, Carlsbad, USA). Secondary antibodies were donkey anti-mouse Alexafluor 488, 594 and donkey anti-rabbit Alexafluor 594, all from Invitrogen (1/1000). For nuclear staining, Hoechst 33258 (1/1000, Sigma-Aldrich, Taufkirchen, Germany) was used. For immunostaining of YAP, rabbit polyclonal YAP antibody (1/200, #4912, Cell Signaling, Danvers, USA) and DAB substrate (Roche Diagnostics Inc, Manheim, Germany) were used. Samples were examined with a fluorescence microscope (BX51and DP80, Olympus, Tokyo, Japan) using cellSens software (Olympus, Tokyo, Japan). After H&E staining, the areas of living layer and stratum corneum were calculated using ImageJ 1.47 v (NIH, Bethesda, MD, USA).

Electron-microscopic observation

As describe in chapter 2, Epidermal model samples for electron microscopy were minced (< 0.5 mm^3 pieces), fixed overnight in modified Karnovsky's fixative, post-fixed in 2% aqueous osmium tetroxide or 0.2% ruthenium tetroxide, dehydrated in graded ethanol solutions, and embedded in Epon-epoxy mixture.

Trans epidermal water loss

As describe in chapter 3, TEWL was measured as described by Hanley *et al.* (90), Inserts with epidermal models were placed dermis-side down onto silicon rubber plates and the lateral edges were sealed with petrolatum, so that water loss occurred only through the epidermal surface. Epidermis model sections were kept at ambient temperature (37 °C) and low humidity (< 5%), and weighed for 2 hours. TEWL levels are reported as milligrams of water lost per square millimeter per hour. Epidermal model sections from four different subjects were used. I used 6 control (on flat membrane) models and 6 models on textile #255. Each sample was taken from an independent model.

Statistics

The results are expressed as the mean ± SD. Statistical significance of differences between two groups was determined by a two-tailed Student's t-test. In the case of more than 2 groups, statistical significance was determined by ANOVA with Tukey's honestly

significant difference (HSD), using KaleidaGraph (HULINKS, Tokyo, Japan). P-values less than 0.05 were considered significant.

5-3. Results

The results of the new three-dimensional computer simulation and the cultured epidermal models are illustrated in Figure 5-1(a-e). Compared with the result obtained using a flat basement membrane (Figure 5-1(a)), the SC and living layer were thicker on the sinusoidal basement membrane (Figure 5-1(b)). The numbers of cells in the SC and the living layer of the epidermis in the two cases are shown on the right. To validate the simulation results, I attempted to construct a thick epidermal model with passaged keratinocytes by using an appropriately patterned substrate. For this purpose, I seeded keratinocytes on a series of textile samples with different textures in culture dishes. For comparison with the textile pattern parameters (Table. 5-1, Supplement Figure 5-1), I also measured the corresponding values of human papillary layer, which exhibited a rete ridge height (corresponding to fiber thickness) of 51 μm and an undulation interval (fiber interval) of 105 μm (n = 13, abdominal skin, average age of subjects 36.3 years). Representative microscopic H&E-stained images of the grown epidermal models are shown in Figure 5-1(c). The results of quantification of the living layer of epidermis and SC are shown in Figure 5-1(d, e), respectively (no epidermal sheet developed on samples #74, #86, #125, and #160). Textiles #200, #255 and #300 afforded significantly thicker SC than the control (no textile). The living layer of epidermis on textile #255 was thicker than that on textile #200 (statistically significant) or #300 (not significant). Therefore, we focused on textile #255 for further study.

Structural proteins filaggrin, loricrin, claudin 1 and ZO-1 play key roles in epidermis (121, 122) so to confirm that they were appropriately expressed, I carried out immuno-histochemical studies of epidermal models grown on textile #255. As shown in Figure 5-2, differentiation markers filaggrin (Figure 5-2(a)) and loricrin (Figure 5-2(b)) and tight-junction markers ZO-1 (Figure 5-2(c)) were all appropriately expressed at the upper layer of the epidermis. Claudin 1 was expressed in the cell membrane throughout the epidermis (Figure 5-2(d)). In addition, electron-microscopic images revealed thick SC (Figure 5-2(f), black asterisk) containing intercellular lipid bilayer structure (Figure 5-2(g), black asterisk), suggesting that the model would show effective barrier function. Immunohistochemical studies of the model grown on textile #300 and the control are shown in supplement Figure 5-2. ZO-1 and claudin 1 were expressed in both cases, though expression of ZO-1 seemed weaker in the model grown on textile #300 than in that grown on textile #255. To confirm this, I measured TEWL of control and epidermal

models (Figure 5-2(h)). Compared with the control, epidermal models grown on textile #255 showed significantly lower TEWL, indicating that they have greater barrier function. In the present proof-of-concept study, we focused on TEWL to evaluate the skin equivalent model because it is widely used as a parameter of epidermal water-impermeable barrier function, which is critical for the present purpose. Anti-BrdU staining revealed that proliferating cells were present only at the bottom in the control (Figure 5-3(a) no textile), whereas proliferating cells were also observed on fibers of the textile substrate in the experimental model (Figure 5-3(b), black arrows). I also examined expression of MCSP, which plays a role in stabilizing cell-substratum interactions (123). Anti-MCSP immunostaining revealed positive cells on fibers (Figure 5-3(d), white arrows), supporting the idea that at least some cells on fibers had proliferative ability. Supplement Figure 5-3 shows the results of double immunohistochemical staining with anti-BrdU and K14, a basal-layer marker, of the model grown on textile #255 and the no-textile control. Co-expression of BrdU and K14 was observed on the top of the fibers in the model, suggesting that proliferating cells may recognize the top of the fibers as a basal layer.

I next examined the role of the key transcriptional regulator YAP in the present model by employing siRNA. In control epidermis, YAP was localized only at the basal layer (Figure 5-3(e)), while in the textile-grown model, YAP was expressed around fibers (Figure 5-3(f), red arrows). Representative images are shown in Figure 5-3(g-j). Application of YAP siRNA markedly disturbed the formation of three-dimensional structure, as can be seen by comparison of H&E staining of control and YAP siRNA-applied textile-grown samples (Figure 5-3(g, h) respectively). In control siRNA-treated epidermis, YAP was expressed around fibers (Figure 5-3(i)), while little expression was observed in YAP siRNA-treated samples (Figure 5-3(j)). Application of YAP siRNA did not influence proliferation of keratinocytes in monolayer culture (data not shown). YAP siRNA application also disturbed construction of three-dimensional structure in the control model. The precise role of YAP in construction of the thicker epidermal model remains to be established.

5-4. Discussion

The in vitro results confirmed Nagayama *et al.* in-silico prediction that undulation of the basement membrane is critical for formation of thick stratum and epidermal living layer. Indeed, the living layer of epidermis and the SC in the epidermal model were thickest when we used textile substrate having an undulation pattern whose spatial scale was comparable to that predicted to be most effective by the computer simulation. Notably, this pattern is also similar to that of the human skin papillary layer in 36-year-old healthy subjects. I also observed BrdU staining and expression of MCSP on cells located on textile fibers in our model, suggesting that cell contact with the textile fibers might promote proliferation. The size and geometry of cells contribute to construction of tissue structure, because they influence intracellular biochemical patterns in multi-cellular systems (124). In addition, the spatial environment of bronchial epithelial cells influences proliferation rate (125). These results are thus consistent with the idea that the spatial features of the basal layer of epidermis play a key role in epidermal structure development and homeostasis, and therefore that the substrate textile pattern is crucial for construction of a thick epidermal model in my system. Further, since rete ridge height decreases with aging (126) and epidermal permeability barrier recovery becomes slower with aging (127), it will be interesting to investigate whether aging-related changes of the undulation pattern of the basal layer are associated with impaired epidermal structure.

YAP is a transcriptional regulator associated with proliferation (128). It is important in constructing three-dimensional body shape (129) and in mechanotransduction (130). In epidermis, YAP is involved in stem cell proliferation (131), terminal differentiation, epidermal permeability-barrier formation (132) and wound healing (133). These findings indicate that YAP may also play a critical role in the development of thick three-dimensional structure in our epidermal-equivalent model, though the mechanism involved remains to be determined.

This work has confirmed the practical value of our mathematical model for guiding the establishment of an epidermal equivalent model with a thick epidermal living layer and thick stratum corneum using passaged keratinocytes. Although other methods are available to construct 3D epidermal equivalent models, as recently reviewed (134), they have limitations. Various scaffold-based 3D models are available, but all of them require a hydrogel scaffold, which our model does not. A scaffold-free 3D methodology has been described, but can only construct micro-scale models, so its usefulness is limited.

Although I focused on TEWL to evaluate our model, and did not carry out further evaluation of the barrier function, I believe my work provides a proof-of-concept of new methodology for the production of physiologically realistic epidermal-equivalent models having a full-thickness epidermal layer that displays signs of differentiation, tight junctions and SC with intercellular lipid bilayer structure, using passaged keratinocytes. Here, we used keratinocytes after three passages, which provided a 512-fold increase of cell number. This should make it possible to construct low-cost epidermal-equivalent models while retaining high quality, although further optimization and validation studies will be necessary. These findings nicely illustrate the utility of in-silico modeling of complex biological processes, since model parameters and conditions can be easily and inexpensively modified in computer simulations.

5-5. Figures

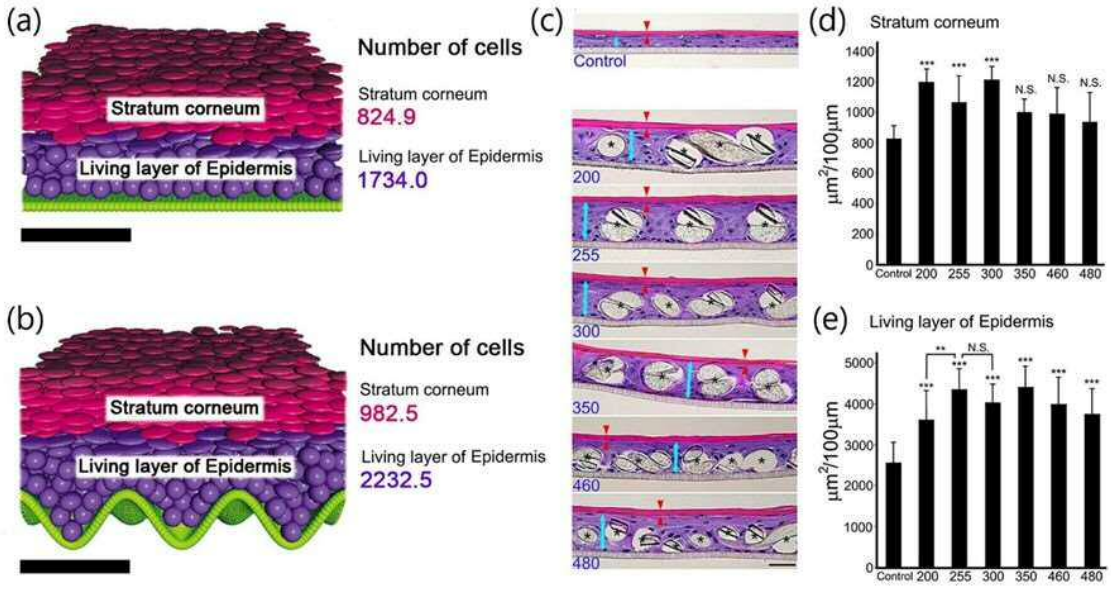

Figure 5-1.

Results of computer simulations of epidermal growth on a flat basement membrane (a) and a sinusoidal basement membrane. (b) ROI: x: 300 μm, y: 300 μm. Numbers of cells in stratum corneum and living layer of each models are indicated on the right. Basement membrane, green; living keratinocytes, purple; cornified cells, red. Bars = 100 μm. Representative images of epidermal-equivalent models. (c) Number at the bottom of each image is the substrate textile number (see Table 1). Living layers are indicated by blue arrows, and stratum corneum by red arrows. Asterisks indicate cross sections of fibers. Bars = 50 μm. (d) Quantified results of stratum corneum area per 100 μm of section (n = 4-6, ANOVA F value = 10.489123, $P < 0.0001$). (e) Quantified results of living layers area per 100 μm of section (n = 4-6, ANOVA F value = 19.154106, $P < 0.0001$). ***$P < 0.0001$, Mean + SD.

Table 1 Properties of polyester textile samples used as substrates

Identification No. of textile	Fiber thickness (μm)	Inter-fiber interval (μm)
74	205	354
86	165	301
125	122	201
160	100	164
200	73	127
255	60	101
300	51	87.6
350	60	75.2
460	41	57.5
480	55	52.9

Table 1.

Properties of polyester textile samples used as substrates.

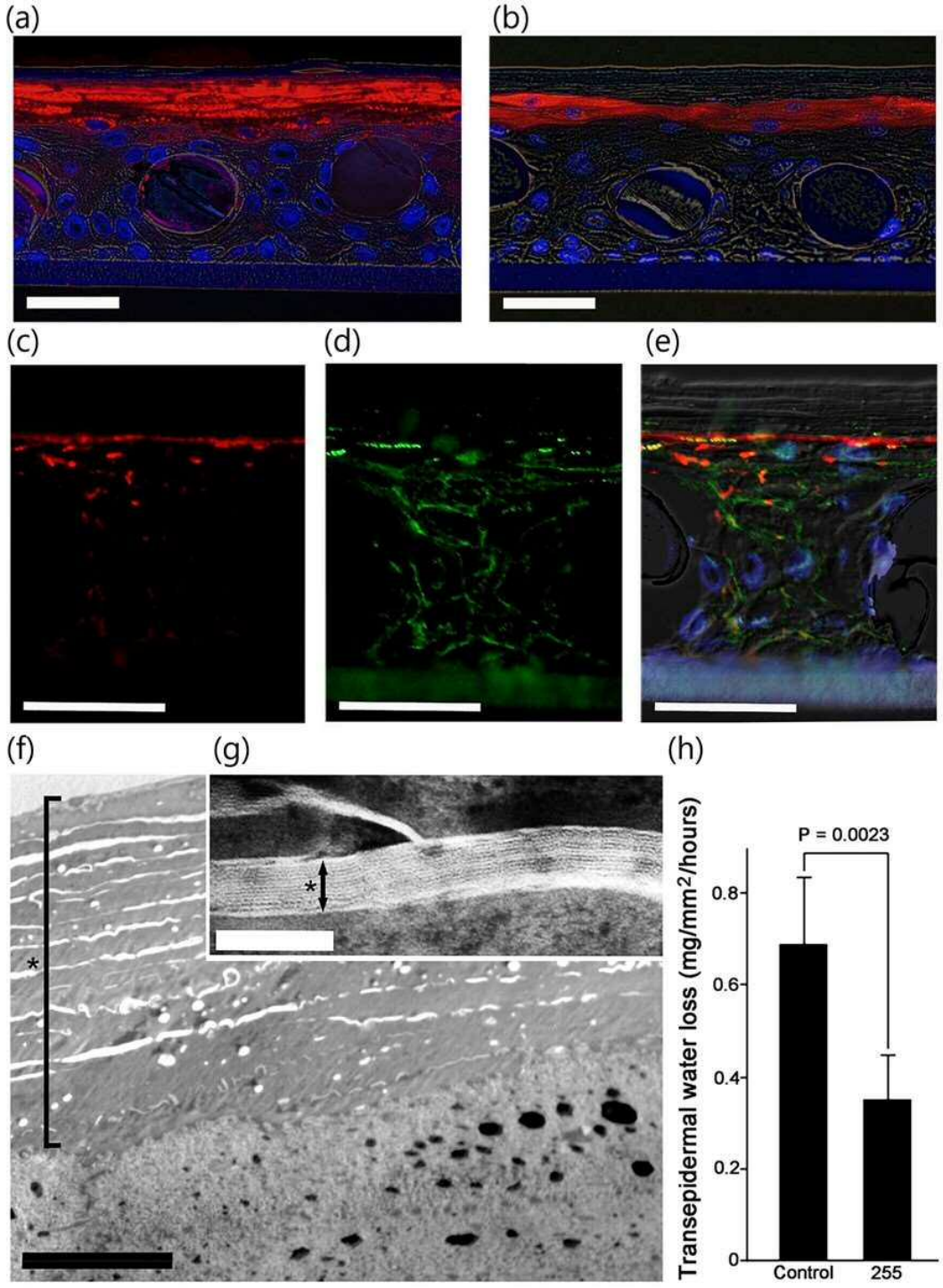
(a)
(b)
(c)
(d)
(e)
(f)
(g)
(h)
*
*
P = 0.0023
Transepidermal water loss (mg/mm2/hours)
0
0.2
0.4
0.6
0.8
Control
255

Figure 5-2.

Immunostaining and electro-microscopic observation. Differentiation markers filaggrin (a) and loricrin (b) are expressed at the uppermost layer of epidermis. Tight junction markers ZO-1 (c) are expressed at the upper layer of the epidermis and claudin 1 (d) are expressed at the cell membrane throughout the epidermis. (e) Merged image of c and d. Bars = 20 μm. (f, g) Electron-microscopic images of model grown on textile #255. Thick stratum corneum was observed (f, black asterisk; bar = 5 μm) and contained intercellular lipid bilayer structure (g, black asterisk, bar = 100 nm). Transepidermal water loss of control and epidermal models grown on textile #255 (h). Models grown on textile #255 showed significantly lower TEWL. Mean + SD. n = 6.

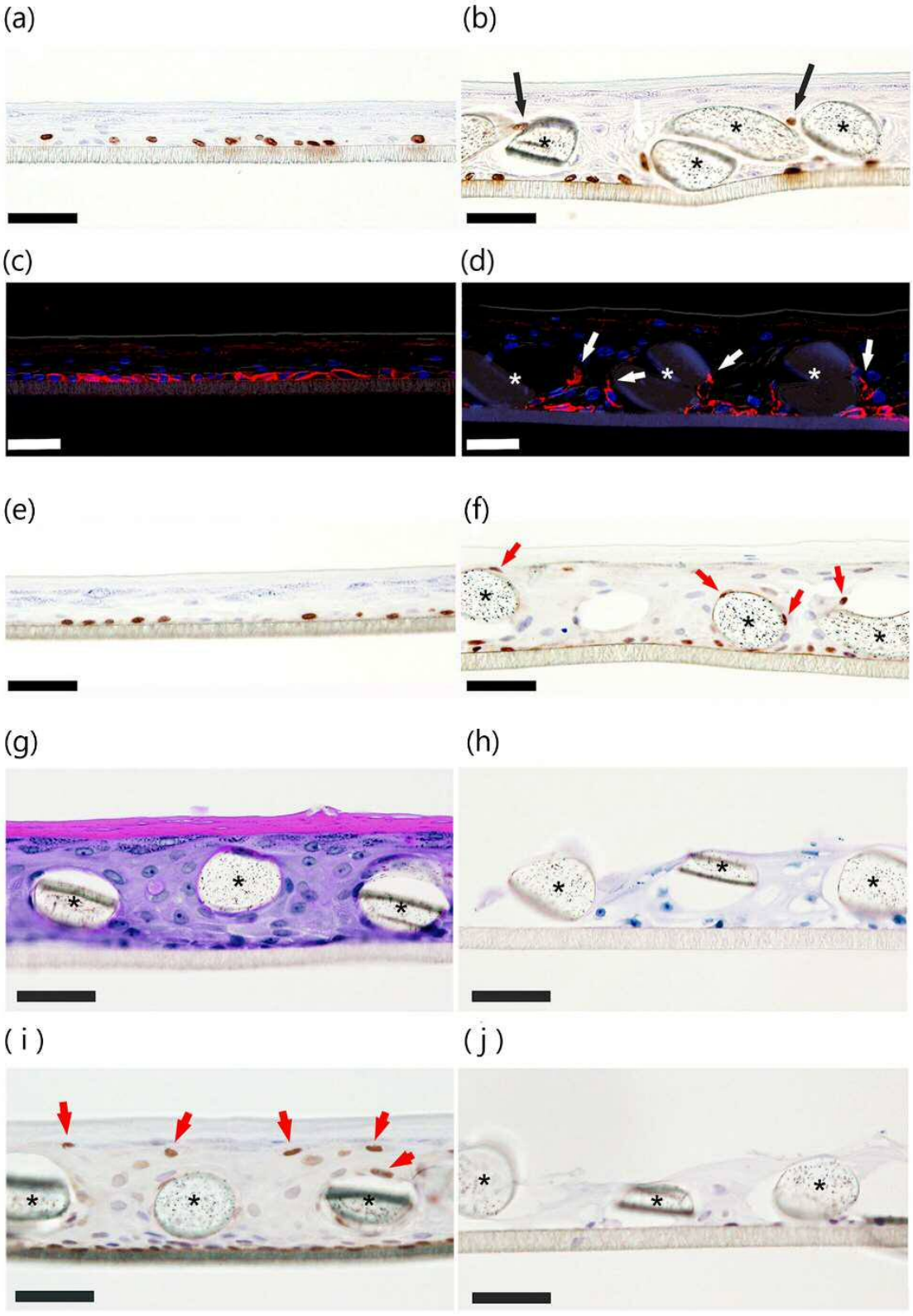
(a)
(b)
(c)
(d)
(e)
(f)
(g)
(h)
(i)
(j)

Figure 5-3.

Proliferation markers and role of YAP. (a, b) Anti-BrdU staining ((a), control; (b), #255 textile, black asterisks indicate cross sections of fibers.). In the control, proliferating cells appear only at the bottom. Proliferating cells appear at fiber surfaces in B (black arrows). (c, d) Anti-MCSP immunostaining ((c), control; (d), #255 textile, white asterisks indicate cross sections of fibers). MCSP-positive cells appear on fibers (white arrows). (e, f) Anti-YAP immunostaining ((e), control; (f), #255 textile). YAP-positive cells appear on fibers (red arrows). (g-j) Effects of YAP siRNA (#255 textile). (g, h) H&E staining. (g) Control shows thick epidermis and stratum corneum. (h) YAP siRNA application disturbed structure formation. (i, j) Anti-YAP immunostaining. (i) YAP is expressed on fibers in control (red arrows). (j) Very little YAP expression was observed in YAP siRNA-applied sample. Black asterisks indicate cross sections of fibers. Bars = 50 μm.

Supplement 5-1. Computer simulation.

Simulations are based on a previously proposed model (60), which was extended in the present work in order to incorporate the flattening of epidermal cells. The equations forming the complete model are given below.

In this model, a cell is represented as a spheroid. A cell i has ten variables ($\boldsymbol{x}_i(t)$, $r_i(t)$, $S_i(t)$, $\phi_i(t)$, $c_i(t)$, $P_i(t)$, $h_i(t)$, $v_i^{(\mathrm{p})}(t)$, $v_i^{(\mathrm{r})}(t)$, $\boldsymbol{n}_i(t)$): $\boldsymbol{x}_i(t)$ denotes the position of the cell, $r_i(t)$, the original radius of the cell, $S_i(t)$ the differentiation state variable, $\phi_i(t)$ the phase of the cell division cycle, $c_i(t)$ the intracytoplasmic calcium concentration, P_i(t) the IP_3 concentration, $h_i(t)$ the inactivation factor, $v_i^{(\mathrm{p})}(t)$ and $v_i^{(\mathrm{r})}(t)$ the synthesized and secreted lipid quantity and $\boldsymbol{n}_i(t)$ the direction of the symmetry axis of the cell. The differentiation state of the cell is determined by $S_i(t)$: the cell is in the basal layer if $S_i(t) = 0$, a prickle cell if $0 < S_i(t) < S_g$, and a granular cell if $S_g \leq S_i(t) < S_c$. The cell cornifies when $S_c \leq S_i(t)$. Here, the threshold values S_g and S_c are set as $S_g = 3.0$ and $S_c = 22.0$. We fix the radius $r_i(t)$ to a constant value: $r_i = 2.0$. The length of the symmetry axis of the cell is r_i / α_i^2 and the other two axes are $\alpha_i r_i$. The parameter $\alpha_i = \alpha_i(S)$ is called the flattening rate of the cell, which depends on the differentiation state variable S_i and is governed by equation (1.1). We set $\alpha_{\mathrm{flat}}^{(\max)} = 1.6$ and $\beta_{\mathrm{flat}} = 1.0$. The direction $\boldsymbol{n}_i(t)$ is always normalized and evolves according to equation (1.2), where we denote by $\boldsymbol{v}_i$ the velocity of the i-th cell. We set $\tau_{\boldsymbol{n}} = 0.001$ and $\alpha_{\boldsymbol{n}} = 1.0$.

The cell movement model

The position of the i-th cell $\boldsymbol{x}_i(t)$ is defined in a three-dimensional box $\Omega = [0, L_x] \times [0, L_y] \times [0, L_z]$, where we set $L_x = L_y = 60$ and $L_z = 100$. The movement of the cell depends on the cell type: the governing differential equations are equations (1.3), (1.4) and (1.5) when the cell is a stem cell, transit amplifying (TA) cell and supra-basal cell, respectively. Here we denote by Ω_j the set of all neighbouring cells and particles forming the basal membrane neighbouring the j-th cell. We consider the k-th cell as neighbouring the j-th cell if the distance between these cells is less than or equal to $1.2(\tilde{r}_j + \tilde{r}_k)$, where $\tilde{r}_j$ and $\tilde{r}_k$ are the effective radii of the j-th and k-th cells, respectively, defined as in (1.9). The set of all neighbouring basal membrane particles is denoted by Ω_j^{memb}.

$\boldsymbol{f}_{\mathrm{contact}}$ is the interacting force between neighbouring cells. This force is divided into a Lennard-Jones type repulsive force $\boldsymbol{f}_{\mathrm{LJ}}$ and an adhesion force $\boldsymbol{f}_{\mathrm{adhesion}}$, as shown in equation (1.6).

The Lennard-Jones type force $\boldsymbol{f}_{\mathrm{LJ}}$ is introduced in order to express the excluded volume effect and is given by equations (1.7) and (1.8). Here $\tilde{r}_j$ and $\tilde{r}_k$ are called the

effective radii of cells j and k defined according to equation (1.9). This quantity is introduced because the cell is assumed to be spheroidal. We set $\varepsilon_{LJ} = 0.02$ and $F_{max} = 50$.

The adhesion force $\boldsymbol{f}_{adhesion}$ is given by equations (1.10), (1.11) and (1.12). Here l^* is a parameter which gives the region encompassed by the adhesion force, and is chosen as $l^* = 1.2$. The coefficient $K_{adhesion}$ depends on whether both cells are granular cells or not. The coefficients K_{total} and $K_{desmosome}$ are set as $K_{total} = 7.0$ and $K_{desmosome} = 0.21$, respectively.

The forces $\boldsymbol{f}_{basal}^{(s)}$ and $\boldsymbol{f}_{basal}^{(d)}$ represent the interaction force of the stem cell and the TA cell from the basal membrane, respectively. These forces are defined according to equations (1.13) and (1.14). We set $K_s = 25.0$ and $K_d = 5.0$.

The force $\boldsymbol{f}_{pair}$ acts when a cell is undergoing division and represents the interaction force with the paired cell. The parameter χ_j is equal to 1 if cell division is underway and 0 otherwise. $\boldsymbol{f}_{pair}$ is defined according to equation (1.15) and we set $K_{div} = 5.0$, $R_{max} = 2.0$ and $\varepsilon_L = 0.14$.

The cell differentiation model

Cell differentiation is driven by the intracytoplasmic calcium concentration. The differentiation state variable S_i is governed by (1.16), which changes its behaviour according to whether the cell is cornified or not. c_{out} reflects the advance of differentiation in the presence of extra-cellular calcium and is set as $c_{out} = 1.0 \times 10^{-3}$. We set $\beta_S = 1.5$, $\tau_s = 20$, $c_d = 0.1$ and $\tau_c = 20$. A cornified cell desquamates if S_i exceeds $S_{SC} = 31.3$ and if the number of neighbouring cells is less than 17. It should be noted that we determine the correspondence between the time-scale in real skin and that in our simulation by assuming that a cornified cell desquamates 14 days after it has cornified.

The cell division model

Cell division is governed by the phase parameter $\phi_i(t)$, satisfying the differential equation (1.17). Cell division occurs with a certain probability if $\phi(t)$ exceeds the threshold S_{div}. We set the averaged cell cycle as 4 days in TA cells and 18 days in stem cells.

When the i-th cell is divided into two cells labelled j and k at time t_0, the initial positions are the same: $\boldsymbol{x}_j(t_0) = \boldsymbol{x}_k(t_0)$. We assume that the division is complete if $\| \boldsymbol{x}_j(t) - \boldsymbol{x}_k(t) \| > 1.8R_{max}$.

A stem cell can reproduce an infinite number of times, while a TA cell can reproduce only a finite number of times. We set this maximum reproducing number of TA cells to

be 10.

We also assume that a stem cell is tightly bound to the basal membrane. On the other hand, a TA cell is comparatively loosely bound and can migrate to the supra-basal layer. We consider that once a TA cell leaves the basal layer, it starts its differentiation process.

The lipid dynamics model

The synthesized and secreted lipid quantities $v_i^{(\mathrm{p})}$ and $v_i^{(\mathrm{r})}$ satisfy equations (1.19) and (1.20). The parameters are chosen as follows: $v_{max}^{(p)} = 1$, $c_0 = 0.45$, $k^{(\mathrm{p})}=0.6$, $\sigma_{r1} = 0.1$, $\sigma_{r2} = 0.1$ and $k^{(\mathrm{r})} = 0.2$, $\tau_{\mathrm{p}} = 1.0$, $\tau_{\mathrm{s}} = 1.0$.

The extracellular stimulant dynamics model

In (6), we assumed that an extra-cellular stimulant is released by a cell when it cornifies and that this stimulant induces calcium excitation. The concentration of this stimulant $B(t,x)$ is governed by the diffusion equation (1.21). The parameters are chosen as follows: $d_b = 0.00126$, $K_{bb} = 0.025$, $S_1 = 21.5$ and $S_2 = 24$. We impose the periodic boundary condition in the x and y directions and the Neumann condition in the z direction to solve this partial differential equation.

The calcium dynamics model

The dynamics of $c_i(t)$, $P_i(t)$ and $h_i(t)$ is governed by the equations (1.21). Here $A(t, x)$ denotes the extracellular ATP concentration, and w_{ij} the activity of the gap-junctions between cell i and cell j. The constants in this model are chosen as follows: $d_A = 1.4$, $K_{aa} = 0.5$, $K_{ac} = 0.002$, $d_c = 0.01$, $\delta_I = 1.5$, $K_f = 8.1$, $\mu_0 = 0.567$, $\mu_1 = 0.1$, $K\mu = 0.05$, $\alpha_0 = 0.11$, $K_1 = 0.7$, $\gamma = 2.0$, $K_\gamma = 0.1$, $\beta = 0.02$, $K_{bc} = 0.48$, $H_b = 0.01$, $H_0 = 0.5$, $K_2 = 0.7$, $\varepsilon_{w0} = 0.1$, $w_{d0} = 0.1$, $\tau_g = 0.2$, $\tau_s = 1.0$, $\delta_t = 1.0$, $\delta_I = 1.5$, $k_g = 4.0$, $k_s = 6.0$ and $\delta_k = 1.0$. When calculating $A(t, x)$, we impose the periodic boundary condition in the x and y directions and the Neumann boundary condition in the z direction.

Basement membrane

The basement membrane is expressed as a set of particles whose radii are all equal to 1.0. In the flat case, the membrane is fixed at the plane $z = 0$; in the curved case, the coordinate (x, y, z) of the membrane particle satisfies $z = 5.0 \cos(6\pi x/L_x) \cos(6\pi y/L_y)$. The number of membrane particles is fixed to 16560.

Numerical simulation

For numerical simulation, we set the time step $\Delta t = 0.01$. For particle dynamics, we impose the periodic boundary condition in the x and y directions. We confirmed that L_z is sufficiently large that the uppermost particles desquamate before reaching $z = L_z$. The timescale of calcium dynamics is far faster than that of cell division, migration and differentiation. Accordingly, we calculate the dynamics of cells and the stimulant $B(t, x)$ with the calcium levels kept constant. The calcium dynamics is calculated when a certain number of cells (we choose 20 in our simulations) cornify. In calcium calculation, we regarded $\boldsymbol{x}_i(t)$, $S_i(t)$, $\phi_i(t)$, $B(t, \boldsymbol{x})$ as constant and the calculation is continued until the system reaches a steady state. The two phases of cell dynamics calculation and calcium calculation are repeated.

1 Full model equations

Here and henceforth, $\chi(r)$ denotes the Heaviside step function:

$$\chi(r) := \begin{cases} 1, & r > 0, \\ 0, & r \leq 0. \end{cases}$$

and $x_+ = \max(x, 0)$.

1.1 Cell deformation model

The flattening rate is described as follows:

$$\alpha_i = \alpha(S_i) := \frac{1 + \alpha_{\text{flat}}^{(\max)} \beta_{\text{flat}} S_i^2}{1 + \beta_{\text{flat}} S_i^2}. \tag{1.1}$$

The deformation direction $\boldsymbol{n}_i$ of the i-th cell is given by the following equation:

$$\tau_{\boldsymbol{n}} \frac{d}{dt} \boldsymbol{n}_i = \begin{cases} (\boldsymbol{v}_i(t) - \boldsymbol{n}_i(t)), & \text{if } \|\boldsymbol{v}_i(t) - \boldsymbol{n}_i(t)\| < \alpha_{\boldsymbol{n}}, \\ \alpha_{\boldsymbol{n}} \dfrac{\boldsymbol{v}_i(t) - \boldsymbol{n}_i(t)}{\|\boldsymbol{v}_i(t) - \boldsymbol{n}_i(t)\|}, & \text{if } \|\boldsymbol{v}_i(t) - \boldsymbol{n}_i(t)\| \geq \alpha_{\boldsymbol{n}}, \end{cases} \tag{1.2}$$

where $\boldsymbol{v}_i(t)$ is the velocity of the i-th cell, which is given by the cell movement model. Then a cell C_i is described as a spheroid:

$$\begin{aligned} C_i = \Bigg\{ & (x, y, z); \\ & \frac{1}{\alpha_i^2 r_i^2} \left((x - x_i) \sin\theta_i - (y - y_i) \cos\theta_i \right)^2 \\ & + \frac{1}{\alpha_i^2 r_i^2} \left((x - x_i) \cos\theta_i \sin\varphi_i + (y - y_i) \sin\theta_i \sin\varphi_i - (z - z_i) \cos\varphi_i \right)^2 \\ & + \frac{\alpha_i^4}{r_i^2} \left((x - x_i) \cos\theta_i \cos\varphi_i + (y - y_i) \sin\theta_i \cos\varphi_i + (z - z_i) \sin\varphi_i \right)^2 \leq 1 \Bigg\}, \end{aligned}$$

where $\boldsymbol{x}_i = \begin{pmatrix} x_i \\ y_i \\ z_i \end{pmatrix}$ and $\boldsymbol{n}_i = \begin{pmatrix} \cos\theta_i \cos\varphi_i \\ \sin\theta_i \cos\varphi_i \\ \sin\varphi_i \end{pmatrix}$.

1.2 Cell movement model

$$\frac{d\boldsymbol{x}_j^{(\mathrm{s})}}{dt} = \sum_{k \in \Omega_j} \boldsymbol{f}_{\text{contact}}(\boldsymbol{x}_j^{(\mathrm{s})}, \boldsymbol{x}_k) + \sum_{k \in \Omega_j^{\text{memb}}} \boldsymbol{f}_{\text{basal}}^{(\mathrm{s})}(\boldsymbol{x}_j^{(\mathrm{s})}, \boldsymbol{x}_k^{(\text{memb})}) + \chi_j \boldsymbol{f}_{\text{pair}}(\boldsymbol{x}_j^{(\mathrm{s})}, \boldsymbol{x}_{j'}), \tag{1.3}$$

$$\frac{d\boldsymbol{x}_j^{(\mathrm{d})}}{dt} = \sum_{k \in \Omega_j} \boldsymbol{f}_{\text{contact}}(\boldsymbol{x}_j^{(\mathrm{d})}, \boldsymbol{x}_k) + \sum_{k \in \Omega_j^{\text{memb}}} \boldsymbol{f}_{\text{basal}}^{(\mathrm{d})}(\boldsymbol{x}_j^{(\mathrm{d})}, \boldsymbol{x}_k^{(\text{memb})}) + \chi_j \boldsymbol{f}_{\text{pair}}(\boldsymbol{x}_j^{(\mathrm{d})}, \boldsymbol{x}_{j'}), \tag{1.4}$$

$$\frac{d\boldsymbol{x}_j^{(\mathrm{supra})}}{dt} = \sum_{k\in\Omega_j} \boldsymbol{f}_{\mathrm{contact}}(\boldsymbol{x}_j^{(\mathrm{supra})}, \boldsymbol{x}_k), \tag{1.5}$$

where

$$\begin{aligned}\boldsymbol{f}_{\mathrm{contact}}(\boldsymbol{x}_j, \boldsymbol{x}_k) = \boldsymbol{f}_{\mathrm{LJ}}(\boldsymbol{x}_j, \boldsymbol{x}_k)\chi\left(1 - \frac{\|\boldsymbol{x}_j - \boldsymbol{x}_k\|}{r_j + r_k}\right) \\ + \boldsymbol{f}_{\mathrm{adhesion}}(\boldsymbol{x}_j, \boldsymbol{x}_k, K_{\mathrm{adhesion}})\chi\left(\frac{\|\boldsymbol{x}_j - \boldsymbol{x}_k\|}{r_j + r_k} - 1\right).\end{aligned} \tag{1.6}$$

$$\boldsymbol{f}_{\mathrm{LJ}}(\boldsymbol{x}_j, \boldsymbol{x}_k) := \begin{cases} \boldsymbol{f}_{\mathrm{LJ}}^{(\mathrm{old})}(\boldsymbol{x}_j, \boldsymbol{x}_k), & \text{if } \left|\boldsymbol{f}_{\mathrm{LJ}}^{(\mathrm{old})}(\boldsymbol{x}_j, \boldsymbol{x}_k)\right| \le F_{\max}, \\ F_{\max}\dfrac{\boldsymbol{x}_j - \boldsymbol{x}_k}{\|\boldsymbol{x}_j - \boldsymbol{x}_k\|}, & \text{otherwise.} \end{cases} \tag{1.7}$$

$$\boldsymbol{f}_{\mathrm{LJ}}^{(\mathrm{old})}(\boldsymbol{x}_j, \boldsymbol{x}_k) := \frac{4\epsilon_{\mathrm{LJ}}}{\|\boldsymbol{x}_j - \boldsymbol{x}_k\|}\left[\left(\frac{\widetilde{r}_j + \widetilde{r}_k}{\|\boldsymbol{x}_j - \boldsymbol{x}_k\|}\right)^{12} - \left(\frac{\widetilde{r}_j + \widetilde{r}_k}{\|\boldsymbol{x}_j - \boldsymbol{x}_k\|}\right)^{6}\right]\frac{\boldsymbol{x}_j - \boldsymbol{x}_k}{\|\boldsymbol{x}_j - \boldsymbol{x}_k\|}. \tag{1.8}$$

$$\begin{aligned}\widetilde{r}_j &:= \sqrt{\frac{r_j^2}{\alpha_j^4}\cos^2\theta_j + \alpha_j^2 r_j^4 \sin^2\theta_j}, \\ \theta_j &:= \arccos\left(\frac{(\boldsymbol{x}_k - \boldsymbol{x}_j)}{\|\boldsymbol{x}_k - \boldsymbol{x}_j\|}\cdot\boldsymbol{n}_j\right).\end{aligned} \tag{1.9}$$

$$\begin{aligned}&\boldsymbol{f}_{\mathrm{adhesion}}(\boldsymbol{x}_j, \boldsymbol{x}_k, K_{\mathrm{adhesion}}) \\ &= \begin{cases} -K_{\mathrm{adhesion}} f\left(\dfrac{\|\boldsymbol{x}_j - \boldsymbol{x}_k\|}{\widetilde{r}_j + \widetilde{r}_k} - 1\right)\dfrac{\boldsymbol{x}_j - \boldsymbol{x}_k}{\|\boldsymbol{x}_j - \boldsymbol{x}_k\|}, & \text{if } \dfrac{\|\boldsymbol{x}_j - \boldsymbol{x}_k\|}{\widetilde{r}_j + \widetilde{r}_k} < l^*, \\ 0, & \text{otherwise,} \end{cases}\end{aligned} \tag{1.10}$$

where

$$f(r) = r - \frac{1}{(l^* - 1)^2}r^3, \tag{1.11}$$

$$K_{\mathrm{adhesion}} = \begin{cases} K_{\mathrm{total}}, & \text{if } S_j \ge S_g \text{ and } S_k \ge S_g, \\ K_{\mathrm{desmosome}}, & \text{otherwise,} \end{cases} \tag{1.12}$$

$$\begin{aligned}\boldsymbol{f}_{\mathrm{basal}}^{(\mathrm{s})}(\boldsymbol{x}_j, \boldsymbol{x}_k) = \boldsymbol{f}_{\mathrm{LJ}}(\boldsymbol{x}_j, \boldsymbol{x}_k)\chi\left(1 - \frac{\|\boldsymbol{x}_j - \boldsymbol{x}_k\|}{r_j + r_k}\right) \\ - K_s\frac{\boldsymbol{x}_j - \boldsymbol{x}_k}{\|\boldsymbol{x}_j - \boldsymbol{x}_k\|}\left(\frac{\|\boldsymbol{x}_j - \boldsymbol{x}_k\|}{r_j + r_k} - 1\right)\chi\left(\frac{\|\boldsymbol{x}_j - \boldsymbol{x}_k\|}{r_j + r_k} - 1\right),\end{aligned} \tag{1.13}$$

$$\begin{aligned}\boldsymbol{f}_{\mathrm{basal}}^{(\mathrm{d})}(\boldsymbol{x}_j, \boldsymbol{x}_k) = \boldsymbol{f}_{\mathrm{LJ}}(\boldsymbol{x}_j, \boldsymbol{x}_k)\chi\left(1 - \frac{\|\boldsymbol{x}_j - \boldsymbol{x}_k\|}{r_j + r_k}\right) \\ + \boldsymbol{f}_{\mathrm{adhesion}}(\boldsymbol{x}_j, \boldsymbol{x}_k, K_d)\chi\left(\frac{\|\boldsymbol{x}_j - \boldsymbol{x}_k\|}{r_j + r_k} - 1\right),\end{aligned} \tag{1.14}$$

$$\begin{aligned}\boldsymbol{f}_{\mathrm{pair}}(\boldsymbol{x}_j, \boldsymbol{x}_{j'}) &= -K_{\mathrm{div}}\frac{\boldsymbol{x}_j - \boldsymbol{x}_{j'}}{\|\boldsymbol{x}_j - \boldsymbol{x}_{j'}\|}\left(\|\boldsymbol{x}_j - \boldsymbol{x}_{j'}\| - \ell(t)\right), \\ \frac{d}{dt}\ell(t) &= \epsilon_{\mathrm{L}}(2R_{\max} - \ell(t)).\end{aligned} \tag{1.15}$$

1.3 Cell differentiation model

$$\begin{aligned} &\tau_S \frac{d}{dt} S_i = c_{\text{out}} + \beta_S (c_i - c_0)_+, \quad 0 \le S_i < S_c, \\ &\tau_S \frac{d}{dt} S_i = c_d, \qquad\qquad\qquad\quad S_i \ge S_c. \end{aligned} \tag{1.16}$$

1.4 Cell division model

$$\tau_\phi \frac{d}{dt} \phi_i = \phi_0 + \beta_\phi (c_i - c_0)_+. \tag{1.17}$$

1.5 Lipid dynamics model

$$\begin{cases} \tau_p \dfrac{d}{dt} v_i^{(\mathrm{p})} &= (v_{\max}^{(\mathrm{p})} - v_i^{(p)}) f^{(p)}(c_i, S_i) - v_i^{(p)} f^{(r)}(c_i, S_i), \\ \tau_r \dfrac{d}{dt} v_i^{(r)} &= v_i^{(p)} f^{(r)}(c_i, S_i), \end{cases} \tag{1.18}$$

where

$$f^{(p)}(c_i, S_i) = \frac{k^{(\mathrm{p})}}{4} \left(1 + \tanh\left(\frac{S_i - S_g}{\sigma_{r1}}\right)\right) \left(1 + \tanh\left(\frac{c_0 - c_i}{\sigma_{r2}}\right)\right), \tag{1.19}$$

$$f^{(r)}(c_i, S_i) = \frac{k^{(\mathrm{r})}}{4} \left(1 + \tanh\left(\frac{S_i - S_g}{\sigma_{r1}}\right)\right) \left(1 + \tanh\left(\frac{c_i - c_0}{\sigma_{r2}}\right)\right). \tag{1.20}$$

1.6 Extra-cellular stimulant dynamics model

$$\frac{\partial B}{\partial t} = d_b \Delta B - K_{bb} B + \sum_{i=1}^{N} F_B(S_i, \boldsymbol{x}_i), \tag{1.21}$$

where

$$F_B(S_i, \boldsymbol{x}_i) = \chi(S_i - S_1)\chi(S_2 - S_i)\chi(r - \|\boldsymbol{x} - \boldsymbol{x}_i\|).$$

1.7 Calcium dynamics model

$$\begin{cases} \dfrac{\partial A}{\partial t} &= d_A \Delta A - K_{aa} A + \displaystyle\sum_{i=1}^{N} G\left(\boldsymbol{x}, \boldsymbol{x}_i, \frac{dc_i}{dt}\right), \\ \dfrac{dP_i}{dt} &= \displaystyle\sum_{j \in \Lambda_i} d_P w_{ij} I_n(S_i)(P_j - P_i) + F_P(A, S_i) - K_{pp} P_i, \\ \dfrac{dc_i}{dt} &= \displaystyle\sum_{j \in \Lambda_i} d_c w_{ij} I_n(S_i)(c_j - c_i) + F_c(P_i, c_i, h_i, B), \\ \dfrac{dh_i}{dt} &= \dfrac{1}{\tau_h(S_{k_i})} F_h(c_i, h_i), \\ \dfrac{dw_{ij}}{dt} &= F_w(w_{ij}, c_i, c_j), \end{cases} \tag{1.22}$$

where

$\boldsymbol{x},\ \boldsymbol{x}_i \in \Omega = [0, L_x] \times [0, L_y] \times [0, L_z],\ t > 0,\ i \in \{1, 2, \dots N(t)\}.$

$$G\left(\boldsymbol{x}, \boldsymbol{x}_i, \frac{dc_i}{dt}\right) = K_{ac}\chi(r - \|\boldsymbol{x} - \boldsymbol{x}_i\|)\chi\left(\frac{dc_i}{dt}\right), \tag{1.23}$$

$$F_c(P, c, h, B) = K_f\left(\mu_0 + \frac{\mu_1 P}{K_\mu + P}\right)\left(\alpha_0 + \frac{(1-\alpha_0)c}{K_1 + c}\right)h - \frac{\gamma c}{K_\gamma + c} + \beta + \frac{K_{bc}B^2}{H_b + B^2}, \tag{1.24}$$

$$F_P(A, S_i) = K_{pa}(S_i)\frac{A}{H_0 + A}, \qquad F_h(c, h) = \frac{K_2^2}{K_2^2 + c^2} - h, \tag{1.25}$$

$$F_w(w_{ij}, c_i, c_j) = -w_{ij} + \frac{1}{2}\left(1 + \tanh\left(\frac{w_{d0} - |c_i - c_j|}{\varepsilon_{w0}}\right)\right), \tag{1.26}$$

$$\tau_h(S_i) = \tau_g + \frac{\tau_s - \tau_g}{2}\left(1 + \tanh\left(\frac{S_g - S_i}{\delta_\tau}\right)\right), \tag{1.27}$$

$$I_n(S_i) = \frac{1}{2}\left(1 + \tanh\left(\frac{S_i - S_g}{\delta_I}\right)\right), \tag{1.28}$$

$$K_{pa}(S_i) = k_g + \frac{k_s - k_g}{2}\left(1 + \tanh\left(\frac{S_g - S_i}{\delta_k}\right)\right). \tag{1.29}$$

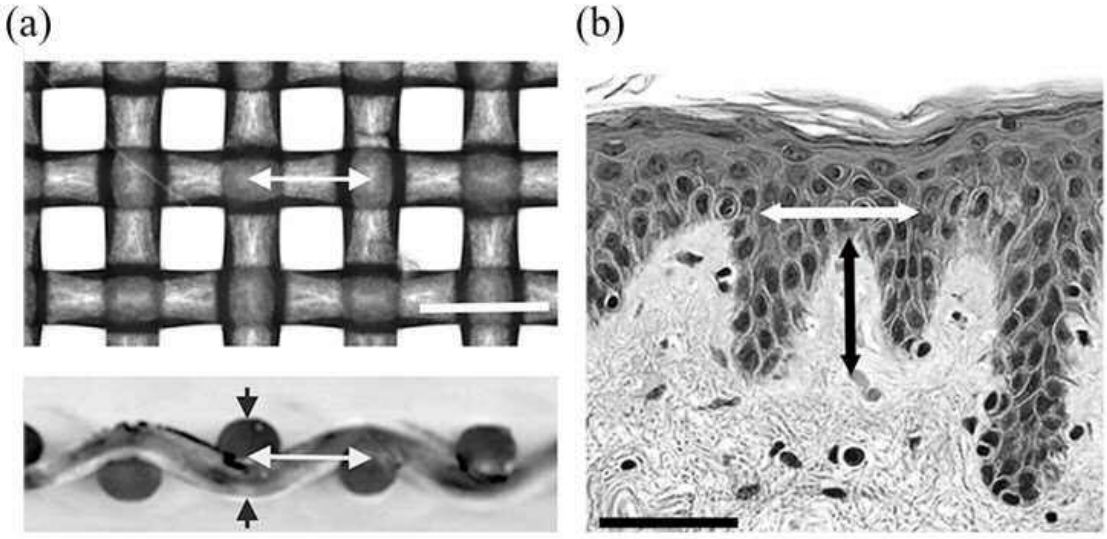

Supplement Figure 5-1.

Evaluation of thickness and inter-fiber interval (undulation) of textile samples and human skin papillary layer. (a) Overhead view of textile #255 (upper image) and cross section of the textile (lower image). White arrows indicate the inter-fiber interval (undulation) of the textile and the thickness of the undulation is indicated by black arrowheads. White bar = 100μm. (b) Corresponding parameters of human epidermis. The undulation interval is indicated by a white arrow and the thickness is indicated by a black arrow.

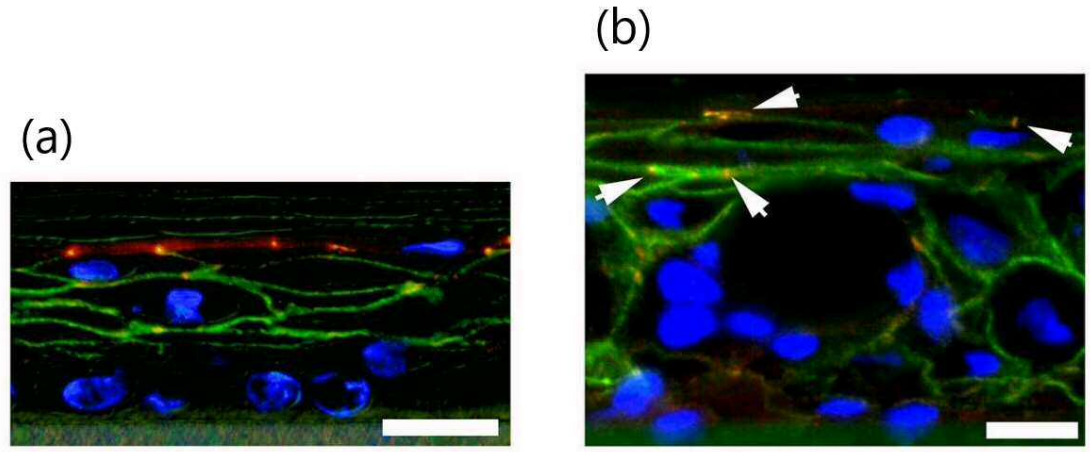

Supplement Figure 5-2.

Merged images of immunostaining with tight junction markers ZO-1 (Red) and claudin 1 (Green) of control (a) and #300 textile (b) models. Bars = 50 μm. In the control, ZO-1 was expressed in the uppermost layer and claudin 1 was expressed in the cell membranes throughout the layers (a). In the case of #300, claudin 1 was expressed in the cell membranes throughout the layers and a little ZO-1 was expressed in the upper layer of the epidermis (b: arrows).

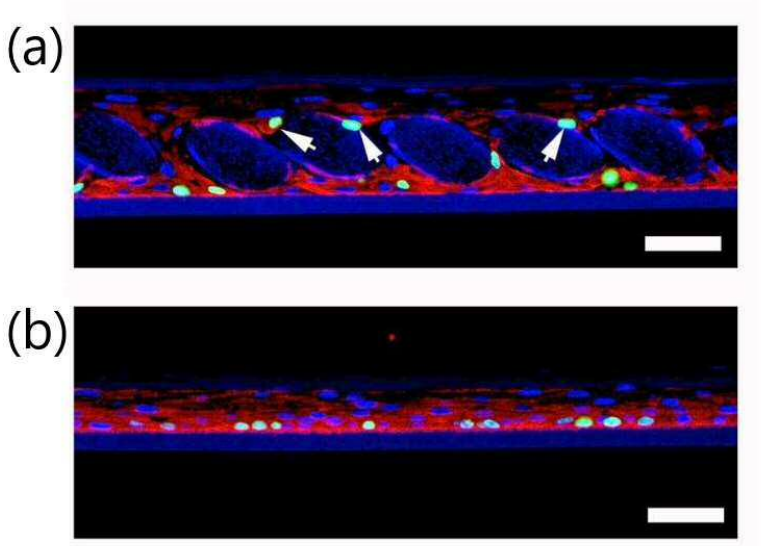

Supplement Figure 5-3.

Merged images of co-immunostaining with K14 (red, basal cell marker, anti-cytokeratin 14 antibody, 1/1000, clone RCK107, # MAB3232, EMD Millipore, Burlington, USA) and BrdU (green) of #255 textile (a) and control (b) models. BrdU-positive cells were localized at the K14-positive area, even on top of the #255 fibers (A: arrows). Bars = 50 μm.

Chapter 6. General Conclusion

The skin has a variety of critical functions: it not only protects the body from exogenous insults, including pathogens, but also serves as a sensory organ that receives multiple types of signals from the outside environment, and provides a barrier function to prevent excessive water loss. The function of the epidermal barrier, which consists of anucleate keratinocytes and intercellular lipids, is maintained homeostatically. Despite many biochemical studies of epidermal barrier function, the mechanisms of associated biophysical phenomena, such as maintenance of the calcium gradient, and the supply of lipids to the SC, remain poorly understood. These questions are important, because inflammatory skin diseases, including atopic dermatitis and psoriasis vulgaris, exhibit abnormalities of this barrier function. In these diseases, the balance of keratinocyte proliferation/differentiation is disrupted by calcium gradient disappear and/or mutation of intracellular calcium dynamics, leading to epidermal barrier hypofunction or dysfunction. Moreover, inflammation can be further exacerbated by allergen contact, mechanical irritation, and dryness, leading to a vicious circle of intractable pathologies (135-138). Until now, although intracellular calcium dynamics of cultured keratinocytes has been well studied, evaluate calcium dynamics and barrier function using human skin tissue are still poorly understood. Therefore, an understanding of the mechanisms of barrier homeostasis and calcium dynamics using human skin tissue might lead to the establishment of new therapeutic methods.

However, the mechanisms for maintaining barrier homeostasis are very complex. One approach to address such phenomena is the use of mathematical models, which can be simplified as necessary. Then, the predictions obtained by computer simulation can be checked experimentally and the model adjusted until satisfactory results are obtained. In this work, therefore, the aim was to establish of new methods for visualization of calcium dynamics and evaluation of epidermal barrier function using cultured human skin by means of a combination of both physiological experiments and mathematical modeling. Four studies were conducted.

The first study (chapter 2) deals with the relationship between barrier function, calcium ion concentration gradient, and electrical potential. Exocytosis of lamellar bodies at the uppermost nucleated layer of the epidermis is a crucial process for epidermal permeability barrier homoeostasis. Denda *et al.* have suggested that skin surface electrical potential might be associated with barrier homoeostasis. Thus, I hypothesized that this potential might be the driver of exocytosis of lamellar bodies. I

tested this idea by applying a negative electric potential (-0.5 V) to human skin tissue samples *ex vivo* for 2 h and monitoring the ultrastructure of the uppermost layer. The secretion of lamellar bodies was accelerated in the potential-applied skin, compared to that in untreated control skin. Multiphoton observation indicated that extracellular lipid domains were more extensive in treated skin than in control skin. Moreover, the calcium ion gradient was greater at the uppermost layer of the epidermis of treated skin, compared to that in control skin. These results are consistent with the idea that electrical potential regulates lamellar body secretion in healthy human skin.

The second study (chapter 3) deals with the effects of allergens on barrier function. Cry j1 is the major peptide allergen of Japanese cedar (Sugi), *Cryptomeria japonica*. I hypothesized that Cry j1 might disrupt epidermal permeability barrier homeostasis, like some other allergens. Furthermore, although a barrier function evaluation method using mice has been established, a barrier function evaluation method using human skin tissue has not been established. Therefore, I established a barrier function evaluation method using human skin tissue and evaluated the effect of Cry j1 on the barrier function. First, I found that application of Cry j1 significantly increased the intracellular calcium level of keratinocytes, as measured with a ratiometric fluorescent probe, Fura-2 AM, and this increase was inhibited by trypsin inhibitor or a PAR-2 antagonist. Then, the effect of Cry j1 on TEWL of cultured human skin tissue was measured in the presence and absence of a trypsin inhibitor and PAR-2 antagonist. Cry j1 significantly impaired the barrier function of human skin *ex vivo*, and this action was blocked by co-application of trypsin inhibitor or PAR-2 antagonist. Moreover, electron-microscopic observation confirmed that Cry j1 blocked lamellar body secretion. These results suggested that interaction of Cry j1 with epidermal keratinocytes leads to the activation of PAR-2, which in turn induces elevation of intracellular calcium and disruption of barrier function. Thus, blocking the interaction of Cry j1 with epidermal keratinocytes might ameliorate the allergic reaction and prevent disruption of epidermal permeability barrier homeostasis.

The focus of the third study (chapter 4) is intraepidermal Ca^{2+} dynamics. Changes of epidermal calcium ion concentration are involved in regulation of barrier homeostasis and keratinocyte differentiation. Moreover, intracellular calcium dynamics might play a role in skin sensation. But, although calcium dynamics of cultured keratinocytes in response to mechanical stresses has been well studied, calcium propagation in stimulated human epidermis is still poorly understood. To investigate this issue, I used a new method for real-time measurement of calcium dynamics in response to point stimulation of human epidermis at the single-cell level. I examined calcium propagation

in cross-sectional samples of living human epidermis *ex vivo*, as well as in cultured human keratinocytes, by means of two-photon microscopy after stimulating cells in the SG with the emission laser of a two-photon microscope. Interestingly, cells in different epidermal layers showed different responses, and those in the SB showed the greatest elevation of intracellular calcium. Calcium propagation in the epidermis was inhibited in the presence of apyrase (which degrades adenosine triphosphate; ATP) or gap-junction blockers. In cultured keratinocytes, on the other hand, calcium propagated in a simple concentric wave-like manner from the stimulation site, and propagation was strongly suppressed by apyrase. These results suggested that ATP and gap junctions play important roles in calcium propagation induced by point laser stimulation of the uppermost layer of epidermis. This method should be broadly useful to study calcium dynamics, epidermal physiological mechanisms, and mechanisms of skin sensation at the single-cell level.

In the fourth study (chapter 5), I conducted computer simulations with a mathematical model in order to predict how an epidermal model with a high SC barrier function might be constructed. Experimental models of human epidermis are useful research tools for elucidate various skin diseases and epidermal functions. However, it has not been able to sufficiently mimic the actual human skin barrier function, and it is difficult to investigate the factors one by one. Therefore, in this study, I aimed to construct an experimental model of human epidermis with a function similar to the human skin barrier by using a mathematical model. The established mathematical model of epidermal homeostasis predicted that the undulatory pattern of the papillary layer beneath the epidermis is a key determinant of epidermal thickness. I tested this prediction by seeding human keratinocytes on polyester textiles with various fiber-structural patterns in culture dishes exposed to air, aiming to develop a more physiologically realistic epidermal model using passaged keratinocytes. Textile substrate with fiber thickness and inter-fiber distance matching the computer predictions afforded a three-dimensional epidermal-equivalent model with thick stratum corneum and intercellular lamellar lipid structure. Cells located around the textile fibers were proliferating, as indicated by BrdU and YAP staining and expression of melanoma-associated chondroitin sulfate proteoglycan. Filaggrin, loricrin, claudin 1 and ZO-1 were all appropriately expressed. Measurement of TEWL indicated that the model has excellent barrier function. These results support the idea that mathematical modeling of complex biological processes can have predictive ability and practical value.

Overall, the results of this work contribute in various ways to our understanding of

the mechanisms of epidermal barrier homeostasis. In particular, I can conclude that the combination of physiological experiments and mathematical models is an effective approach to elucidate the complex mechanisms of barrier homeostasis, as well as to understand the nature of intractable skin diseases, which a key step in developing potential treatments.

Acknowledgments

I am very grateful to Professor Satoshi Nakata of Hiroshima University for encouraging me to take a doctoral degree in the Graduate School of Hiroshima University, and for his constant guidance and valuable advice.

I wish to express my sincere gratitude to Dr. Mitsuhiro Denda (Shiseido Global Innovation Center) for his great interest in this work, well-directed advice, and continuous encouragement.

I would like to express special thanks to Professor Masaharu Nagayama, Hokkaido University, for his encouragement and support throughout this work, as well as to members of the Nagayama JST-CREST team for their support and helpful discussions.

Finally, I sincerely thank my family for their warm and irreplaceable supports.

References

(1) Elias PM. The epidermal permeability barrier: from Saran Wrap to biosensor. In: Elias PM, Feingold KR (eds). *Skin Barrier.* New York, NY: Taylor & Francis; 2006: 25-32.

(2) Denda M, Hosoi J, Asida Y. Visual imaging of ion distribution in human epidermis. *Biochemical and Biophysical Research Communications*. 2000 May 27; 272 (1): 134-7.

(3) Barker AT, Jaffe LF, Vanable JW Jr. The glabrous epidermis of cavies contains a powerful battery. *American Journal of Physiology.* 1982 Mar; 242 (3): R358-66.

(4) Denda M, Ashida Y, Inoue K, Kumazawa N. Skin surface electric potential induced by ion-flux through epidermal cell layers. *Biochemical and Biophysical Research Communications*. 2001 Jun; 284 (1): 112-7.

(5) Kawai E, Nakanishi J, Kumazawa N, Ozawa K, Denda M. Skin surface electric potential as an indicator of skin condition: a new, non-invasive method to evaluate epidermal condition. *Experimental Dermatology*. 2008 Aug; 17 (8): 688-92.

(6) Sakuntabhai A, Ruiz-Perez V, Carter S, Jacobsen N, Burge S, Monk S, Smith M, Munro CS, O'Donovan M, Craddock N, Kucherlapati R, Rees JL, Owen M, Lathrop GM, Monaco AP, Strachan T, Hovnanian A. Mutations in ATP2A2, encoding a Ca^{2+} pump, cause Darier disease. *Nature Genetics*. 1999 Mar; 21 (3): 271-7.

(7) Hu Z, Bonifas JM, Beech J, Bench G, Shigihara T, Ogawa H, Ikeda S, Mauro T, Epstein EH Jr. Mutations in ATP2C1, encoding a calcium pump, cause Hailey-Hailey disease. *Nature Genetics*. 2000 Jan; 24 (1): 61-5.

(8) Denda M, Fujiwara S, Hibino T. Expression of voltage-gated calcium channel subunit alpha1C in epidermal keratinocytes and effects of agonist and antagonists of the channel on skin barrier homeostasis. *Experimental Dermatology*. 2006 Jun; 15 (6): 455-60.

(9) Grando SA. Biological functions of keratinocyte cholinergic receptors. *Journal of Investigative Dermatology Symposium Proceedings*. 1997 Aug; 2 (1): 41-8.

(10) Denda M, Inoue K, Fuziwara S, Denda S. P2X purinergic receptor antagonist accelerates skin barrier repair and prevents epidermal hyperplasia induced by skin barrier disruption. *Journal of Investigative Dermatology*. 2002 Nov; 119 (5): 1034-40.

(11) Denda M, Inoue K, Inomata S, Denda S. gamma-Aminobutyric acid (A) receptor agonists accelerate cutaneous barrier recovery and prevent epidermal hyperplasia induced by barrier disruption. *Journal of Investigative Dermatology*. 2002 Nov; 119 (5): 1041-7.

(12) Denda M, Fuziwara S, Inoue K. Influx of calcium and chloride ions into epidermal keratinocytes regulates exocytosis of epidermal lamellar bodies and skin permeability barrier homeostasis. *Journal of Investigative Dermatology*. 2003 Aug; 121 (2): 362-7.

(13) Denda M, Fuziwara S, Inoue K. Beta2-adrenergic receptor antagonist accelerates skin barrier recovery and reduces epidermal hyperplasia induced by barrier disruption. *Journal of Investigative Dermatology*. 2003 Jul; 121 (1): 142-8.

(14) Fuziwara S, Inoue K, Denda M. NMDA-type glutamate receptor is associated with cutaneous barrier homeostasis. *Journal of Investigative Dermatology*. 2003 Jun; 120 (6): 1023-9.

(15) Fuziwara S, Suzuki A, Inoue K, Denda M. Dopamine D2-like receptor agonists accelerate barrier repair and inhibit the epidermal hyperplasia induced by barrier disruption. *Journal of Investigative Dermatology*. 2005 Oct; 125 (4): 783-9.

(16) Sheikh A, Singh Panesar S, Salvilla S, Dhami S. Hay fever in adolescents and adults. *BMJ Clinical Evidence.* 2009 Nov; 2009: 0509.

(17) Barrera GJ, Tortolero GS. Trefoil factor 3 (TFF3) from human breast milk activates PAR-2 receptors, of the intestinal epithelial cells HT-29, regulating cytokines and defensins. *Bratislavske Lekarske Listy.* 2016; 117 (6): 332-9.

(18) D'Andrea MR, Derian CK, Leturcq D, Baker SM, Brunmark A, Ling P, Darrow AL, Santulli RJ, Brass LF, Andrade-Gordon P. Characterization of protease-activated receptor-2 immunoreactivity in normal human tissues. *Journal of Histochemistry and Cytochemistry.* 1998 Feb; 46 (2): 157-64.

(19) Santulli RJ, Derian CK, Darrow AL, Tomko KA, Eckardt AJ, Seiberg M, Scarborough RM, Andrade-Gordon P. Evidence for the presence of a protease-activated receptor distinct from the thrombin receptor in human keratinocytes. *Proceedings of the National Academy of Sciences of the United States of America*. 1995 Sep 26; 92 (20): 9151-5.

(20) Bando H, Sugiura H, Ohkusa Y, Akahane M, Sano T, Jojima N, Okabe N, Imamura T. Association between first airborne cedar pollen level peak and pollinosis symptom onset: a web-based survey. *International Journal of Environmental Research and Public Health.* 2015; 25 (1): 104-13.

(21) Shinmoto H, Takase M, Naganawa Y, Takano-Ishikawa Y. Production of IgE

antibody to Japanese cedar pollen allergen Cry j1 by short term culture of human peripheral blood lymphocytes. *Human Antibodies.* 2009; 18 (1-2): 41-3.

(22) Sone T, Komiyama N, Shimizu K, Kusakabe T, Morikubo K, Kino K. Cloning and sequencing of cDNA coding for Cry j I, a major allergen of Japanese cedar pollen. *Biochemical and Biophysical Research Communications*. 1994 Mar 15; 199 (2): 619-25.

(23) Demerjian M, Hachem JP, Tschachler E, Denecker G, Declercq W, Vandenabeele P, Mauro T, Hupe M, Crumrine D, Roelandt T, Houben E, Elias PM, Feingold KR. Acute modulations in permeability barrier function regulate epidermal cornification: role of caspase-14 and the protease-activated receptor type 2. *The American Journal of Pathology.* 2008 Jan; 172 (1): 86-97.

(24) Jeong SK, Kim HJ, Youm JK, Ahn SK, Choi EH, Sohn MH, Kim KE, Hong JH, Shin DM, Lee SH. Mite and cockroach allergens activate protease-activated receptor 2 and delay epidermal permeability barrier recovery. *Journal of Investigative Dermatology*. 2008 Aug; 128 (8): 1930-9.

(25) Wang L, Hilliges M, Jernberg T, Wiegleb-Edström D, Johansson O. Protein gene product 9.5-immunoreactive nerve fibres and cells in human skin. *Cell and Tissue Research.* 1990 Jul; 261 (1): 25-33.

(26) Shephered GM. The somatic senses. In: Shephered GM (eds) *Neurobiology*. Oxford University Press, Oxford, 1994 pp 265-293.

(27) Nordin M. Low-threshold mechanoreceptive and nociceptive units with unmyelinated (C) fibres in the human supraorbital nerve. *The Journal of Physiology.* 1990 Jul; 426: 229-40.

(28) Johansson RS, Trulsson M, Olsson KA, Westberg KG. Mechanoreceptor activity from the human face and oral mucosa. *Experimental Brain Research*. 1988; 72 (1): 204-8.

(29) Vallbo A, Olausson H, Wessberg J, Norrsell U. A system of unmyelinated afferents for innocuous mechanoreception in the human skin. *Brain Research.* 1993 Nov 19; 628 (1-2): 301-4.

(30) Vallbo AB, Olausson H, Wessberg J. Unmyelinated afferents constitute a second system coding tactile stimuli of the human hairy skin. *Journal of Neurophysiology.* 1999 Jun; 81 (6): 2753-63.

(31) Loomis JM, Collins CC. Sensitivity to shifts of a point stimulus: an instance of tactile hyperacuity. *Perception & psychophysics.* 1978 Dec; 24 (6): 487-92.

(32) Nakata S. Epidermis of the skin as a self-organizing electrochemical sensor. In: Nakata S (eds). *Chemical Analysis Based on Nonlinearity*. NOVA, New York,

NY, pp 2003: 132-138.

(33) Dhaka A, Viswanath V, Patapoutian A. Trp ion channels and temperature sensation. *Annual Review of Neuroscience.* 2006; 29: 135-61.

(34) Denda M, Tsutsumi M. Roles of transient receptor potential proteins (TRPs) in epidermal keratinocytes Transient Receptor Potential Channels. *Advances in Experimental Medicine and Biology*. 2011; 704: 847-860.

(35) Inoue K, Koizumi S, Fuziwara S, Denda S, Inoue K, Denda M. Functional vanilloid receptors in cultured normal human epidermal keratinocytes. *Biochemical and Biophysical Research Communications.* 2002 Feb 15; 291 (1): 124-9.

(36) Chung MK, Lee H, Mizuno A, Suzuki M, Caterina MJ. TRPV3 and TRPV4 mediate warmth-evoked currents in primary mouse keratinocytes. *Journal of Biological Chemistry.* 2004 May 14; 279 (20): 21569-75.

(37) Caterina MJ, Schumacher MA, Tominaga M, Rosen TA, Levine JD, Julius D. The capsaicin receptor: a heat-activated ion channel in the pain pathway. *Nature*. 1997 Oct 23; 389 (6653): 816-24.

(38) Moqrich A, Hwang SW, Earley TJ, Petrus MJ, Murray AN, Spencer KS, Andahazy M, Story GM, Patapoutian A. Impaired thermosensation in mice lacking TRPV3, a heat and camphor sensor in the skin. *Science*. 2005 Mar 4; 307 (5714): 1468-72.

(39) Chung MK, Lee H, Mizuno A, Suzuki M, Caterina MJ. 2-aminoethoxydiphenyl borate activates and sensitizes the heat-gated ion channel TRPV3. *Journal of Neuroscience*. 2004 Jun 2; 24 (22): 5177-82.

(40) Denda M, Sokabe T, Fukumi-Tominaga T, Tominaga M. Effects of skin surface temperature on epidermal permeability barrier homeostasis. *Journal of Investigative Dermatology*. 2007 Mar; 127 (3): 654-9.

(41) Burnstock G, Williams M. P2 purinergic receptors: modulation of cell function and therapeutic potential. *Journal of Pharmacology and Experimental Therapeutics*. 2000 Dec; 295 (3): 862-9.

(42) Cockayne DA, Hamilton SG, Zhu QM, Dunn PM, Zhong Y, Novakovic S, Malmberg AB, Cain G, Berson A, Kassotakis L, Hedley L, Lachnit WG, Burnstock G, McMahon SB, Ford AP. Urinary bladder hyporeflexia and reduced pain-related behaviour in P2X3-deficient mice. *Nature*. 2000 Oct 26; 407 (6807): 1011-5.

(43) Inoue K, Denda M, Tozaki H, Fujishita K, Koizumi S, Inoue K. Characterization of multiple P2X receptors in cultured normal human epidermal keratinocytes.

Journal of Investigative Dermatology. 2005 Apr; 124 (4): 756-63.

(44) Koizumi S, Fujishita K, Inoue K, Shigemoto-Mogami Y, Tsuda M, Inoue K. Ca2+ waves in keratinocytes are transmitted to sensory neurons: the involvement of extracellular ATP and P2Y2 receptor activation. *Biochemical Journal.* 2004 Jun 1; 380 (Pt 2): 329-38.

(45) Denda M, Denda S. Air-exposed keratinocytes exhibited intracellular calcium oscillation. *Skin Research and Technology*. 2007 May;13(2):195-201.

(46) Slominski A. Neuroendocrine system of the skin. *Dermatology*. 2005; 211 (3): 199-208.

(47) Slominski A, Wortsman J, Luger T, Paus R, Solomon S. Corticotropin releasing hormone and proopiomelanocortin involvement in the cutaneous response to stress. *Physiological Reviews*. 2000 Jul; 80 (3): 979-1020.

(48) Slominski A, Wortsman J. Neuroendocrinology of the skin. *Endocrine Reviews.* 2000 Oct; 21 (5): 457-87.

(49) Slominski A, Wortsman J, Pisarchik A, Zbytek B, Linton EA, Mazurkiewicz JE, Wei ET. Cutaneous expression of corticotropin-releasing hormone (CRH), urocortin, and CRH receptors. *FASEB Journal*. 2001 Aug; 15 (10): 1678-93.

(50) S. Nakaoka, K. Aihara. Stochastic simulation of structured skin cell population dynamics. *Journal of Mathematical Biology*. 2013 Mar; 66 (4-5): 807-835

(51) G. Schaller, M. Meyer-HermannA modelling approach towards epidermal homoeostasis control. *Journal of Theoretical Biology*. 2007 Aug; 247 (3): 554-573.

(52) D. Stekel, J. Rashbass, E. Williams. A computer graphic simulation of squamous epithelium. *Journal of Theoretical Biology*. 1995 Aug; 175 (3): 283-293.

(53) J. Rashbass, D. Stekel, E. Williams. The use of a computer model to simulate epithelial pathologies. *The Journal of Pathology.* 1996; 179 (3): 333-339.

(54) S. Maheswaran, P.M. Speight, P. Hammond. Modeling epithelial cell behavior and organization**.** *IEEE Transactions on NanoBioscience*. 2007 Mar; 6 (1): 77-85.

(55) L.H. Cornelissen, C.W.J. Oomens, J.M. Huyghe, F.P.T. Baaijenset. Mechanisms that play a role in the maintenance of the calcium gradient in the epidermis. *Skin Research and Technology*. 2007 Mar; 13 (4): 369-376.

(56) M.P. Adams, D.G. Mallet, G.J. Pettet. Active regulation of the epidermal calcium profile. *Journal of Theoretical Biology.* 2012 May; 301 (21): 112-121.

(57) N. Grabe, K. Neuber. A multicellular systems biology model predicts epidermal morphology, kinetics and Ca^{2+} flow. *Bioinformatics*. 2005 Jul; 21 (17): 3541-3547.

(58) Kobayashi, Y., Sawabu, Y., Kitahata, H., Denda, M. Nagayama, M. Mathematical model for calcium-assisted epidermal homeostasis. *Journal of Theoretical Biology*. 2016 May; 397 (21): 52-60.

(59) Denda M., Denda S., Tsutsumi M., Goto M., Kumamoto J., Nakatani M., Takei K., Kitahata H., Nakata S., Sawabu Y., Kobayashi Y., Nagayama M. Frontiers in epidermal barrier homeostasis - an approach to mathematical modeling of epidermal calcium dynamics. *Experimental Dermatology.* 2014 Feb; 23 (2): 79-82.

(60) Kobayashi, Y. & Nagayama, M. Mathematical model of epidermal structure. R. S. Anderssen et al. (eds), Applications + Practical Conceptualization + Mathematics = fruitful Innovation, Mathematics for Industry 11, *Springer Japan*., 2016 Sep: 121-126.

(61) Werner Y, Lindberg M. Transepidermal water loss in dry and clinically normal skin in patients with atopic dermatitis. *Acta Dermato-Venerelogica*. 1985; 65 (2):102-5.

(62) Tagami H, Yoshikuni K. Interrelationship between water-barrier and reservoir functions of pathologic stratum corneum. *ARCHIVES OF DERMATOLOGY*. 1985 May; 121 (5): 642-5.

(63) Elias PM, Menon GK. Structural and lipid biochemical correlates of the epidermal permeability barrier. *Advances in Lipid Research*. 1991; 24: 1-26.

(64) Lee SH, Elias PM, Proksch E, Menon GK, Mao-Quiang M, Feingold KR. Calcium and potassium are important regulators of barrier homeostasis in murine epidermis. *Journal of Clinical Investigation*. 1992 Feb; 89 (2): 530-8.

(65) Mauro T, Bench G, Sidderas-Haddad E, Feingold K, Elias P, Cullander C. Acute barrier perturbation abolishes the Ca^{2+} and K^{+} gradients in murine epidermis: quantitative measurement using PIXE. *Journal of Investigative Dermatology*. 1998 Dec; 111 (6): 1198-201.

(66) Denda M, Katagiri C, Hirao T, Maruyama N, Takahashi M. Some magnesium salts and a mixture of magnesium and calcium salts accelerate skin barrier recovery. *Archives of Dermatological Research*. 1999 Oct; 291 (10): 560-3.

(67) Edelberg R. Relation of electrical properties of skin to structure and physiologic state. *Journal of Investigative Dermatology*. 1977 Sep; 69 (3): 324-7.

(68) Mitchell P. Chemiosmotic coupling in oxidative and photosynthetic

phosphorylation. *Biological reviews of the Cambridge Philosophical Society*. 1966 Aug; 41 (3): 445-502.

(69) Denda M, Kumazawa N. Negative electric potential induces alteration of ion gradient and lamellar body secretion in the epidermis, and accelerates skin barrier recovery after barrier disruption. *Journal of Investigative Dermatology*. 2002 Jan; 118 (1): 65-72.

(70) Träuble H, Eibl H. Electrostatic effects on lipid phase transitions: membrane structure and ionic environment. *Proceedings of the National Academy of Sciences of the United States of America.* 1974 Jan; 71 (1): 214-9.

(71) Lee SH, Choi EH, Feingold KR, Jiang S, Ahn SK. Iontophoresis itself on hairless mouse skin induces the loss of the epidermal calcium gradient without skin barrier impairment. *Journal of Investigative Dermatology*. 1998 Jul; 111 (1): 39-43.

(72) Frick M, Bertocchi C, Jennings P, Haller T, Mair N, Singer W, Pfaller W, Ritsch-Marte M, Dietl P. Ca2+ entry is essential for cell strain-induced lamellar body fusion in isolated rat type II pneumocytes. *American Journal of Physiology - Lung Cellular and Molecular Physiology.* 2004 Jan; 286 (1): L210-20.

(73) Miklavc P, Frick M, Wittekindt OH, Haller T, Dietl P. Fusion-activated Ca(2+) entry: an "active zone" of elevated Ca(2+) during the postfusion stage of lamellar body exocytosis in rat type II pneumocytes. *PLOS ONE*. 2010 Jun 8; 5 (6): e10982.

(74) Chattopadhyay S, Sun P, Wang P, Abonyo B, Cross NL, Liu L. Fusion of lamellar body with plasma membrane is driven by the dual action of annexin II tetramer and arachidonic acid. *Journal of Biological Chemistry.* 2003 Oct 10; 278 (41): 39675-83.

(75) Ma AS, Ozers LJ. Annexins I and II show differences in subcellular localization and differentiation-related changes in human epidermal keratinocytes. *Archives of Dermatological Research.* 1996 Sep; 288 (10): 596-603.

(76) Denda M, Nakatani M, Ikeyama K, Tsutsumi M, Denda S. Epidermal keratinocytes as the forefront of the sensory system. *Experimental Dermatology*. 2007 Mar; 16 (3): 157-61.

(77) Denda M, Tsutsumi M, Denda S. Topical application of TRPM8 agonists accelerates skin permeability barrier recovery and reduces epidermal proliferation induced by barrier insult: role of cold-sensitive TRP receptors in epidermal permeability barrier homoeostasis. *Experimental Dermatology*. 2010 Sep; 19 (9): 791-5.

(78) Denda M, Tsutsumi M, Goto M, Ikeyama K, Denda S. Topical application of TRPA1 agonists and brief cold exposure accelerate skin permeability barrier recovery. *Journal of Investigative Dermatology*. 2010 Jul; 130 (7): 1942-5.

(79) Reiss K, Meyer-Hoffert U, Fischer J, Sperrhacke M, Wu Z, Dimitrieva O, Krenek P, Suchanova S, Buryova H, Brauer R, Sedlacek R. Expression and regulation of murine SPINK12, a potential orthologue of human LEKTI2. *Experimental Dermatology.* 2011 Nov; 20 (11): 905-10.

(80) Denda M, Kitamura K, Elias PM, Feingold KR. trans-4-(Aminomethyl) cyclohexane carboxylic acid (T-AMCHA), an anti-fibrinolytic agent, accelerates barrier recovery and prevents the epidermal hyperplasia induced by epidermal injury in hairless mice and humans. *Journal of Investigative Dermatology*. 1997 Jul; 109 (1): 84-90.

(81) Elias PM, Ahn SK, Denda M, Brown BE, Crumrine D, Kimutai LK, Kömüves L, Lee SH, Feingold KR. Modulations in epidermal calcium regulate the expression of differentiation-specific markers. *Journal of Investigative Dermatology*. 2002 Nov; 119 (5): 1128-36.

(82) Menon GK, Price LF, Bommannan B, Elias PM, Feingold KR. Selective obliteration of the epidermal calcium gradient leads to enhanced lamellar body secretion. *Journal of Investigative Dermatology*. 1994 May; 102 (5): 789-95.

(83) Behne MJ, Barry NP, Hanson KM, Aronchik I, Clegg RW, Gratton E, Feingold K, Holleran WM, Elias PM, Mauro TM. Neonatal development of the stratum corneum pH gradient: localization and mechanisms leading to emergence of optimal barrier function. *Journal of Investigative Dermatology*. 2003 Jun; 120 (6): 998-1006.

(84) Tarutani M, Nakajima K, Uchida Y, Takaishi M, Goto-Inoue N, Ikawa M, Setou M, Kinoshita T, Elias PM, Sano S, Maeda Y. GPHR-dependent functions of the Golgi apparatus are essential for the formation of lamellar granules and the skin barrier. *Journal of Investigative Dermatology*. 2012 Aug; 132 (8): 2019-25.

(85) Yokozeki H, Satoh T, Katayama I, Nishioka K. Airborne contact dermatitis due to Japanese cedar pollen. *Contact Dermatitis*. 2007 Apr; 56 (4): 224-8.

(86) Tanaka M, Okada M, Zhen YX, Inamura N, Kitano T, Shirai S, Sakamoto K, Inamura T, Tagami H. Decreased hydration state of the stratum corneum and reduced amino acid content of the skin surface in patients with seasonal allergic rhinitis. *British Journal of Dermatology.* 1998 Oct; 139 (4): 618-21.

(87) Ibrahim AR, Kawamoto S, Aki T, Shimada Y, Rikimaru S, Onishi N, Babiker EE, Oiso I, Hashimoto K, Hayashi T, Ono K. Molecular cloning and

immunochemical characterization of a novel major Japanese cedar pollen allergen belonging to the aspartic protease family. *International Archives of Allergy and Immunology.* 2010; 152 (3): 207-18.

(88) Vinhas R, Cortes L, Cardoso I, Mendes VM, Manadas B, Todo-Bom A, Pires E, Veríssimo P. Pollen proteases compromise the airway epithelial barrier through degradation of transmembrane adhesion proteins and lung bioactive peptides. *Allergy*. 2011 Aug; 66 (8): 1088-98.

(89) Shimada SG, Shimada KA, Collins JG. Scratching behavior in mice induced by the proteinase-activated receptor-2 agonist, SLIGRL-NH2. *European Journal of Pharmacology.* 2006 Jan 20; 530 (3): 281-3.

(90) Hanley K, Rassner U, Elias PM, Williams ML, Feingold KR. Epidermal barrier ontogenesis: maturation in serum-free media and acceleration by glucocorticoids and thyroid hormone but not selected growth factors. *Journal of Investigative Dermatology*. 1996 Mar; 106 (3): 404-11.

(91) Denda M, Sato J, Masuda Y, Tsuchiya T, Koyama J, Kuramoto M, Elias PM, Feingold KR. Exposure to a dry environment enhances epidermal permeability barrier function. *Journal of Investigative Dermatology*. 1998 Nov; 111 (5): 858-63.

(92) Mägert HJ, Drögemüller K, Raghunath M. Serine proteinase inhibitors in the skin: role in homeostasis and disease. *Current Protein and Peptide Science.* 2005 Jun; 6 (3): 241-54.

(93) Chen Y, Yang C, Wang ZJ. Proteinase-activated receptor 2 sensitizes transient receptor potential vanilloid 1, transient receptor potential vanilloid 4, and transient receptor potential ankyrin 1 in paclitaxel-induced neuropathic pain. *Neuroscience*. 2011 Oct 13; 193: 440-51.

(94) Patel KN, Liu Q, Meeker S, Undem BJ, Dong X. Pirt, a TRPV1 modulator, is required for histamine-dependent and -independent itch. *PLOS ONE*. 2011; 6 (5): e20559.

(95) Wilson SR, Gerhold KA, Bifolck-Fisher A, Liu Q, Patel KN, Dong X, Bautista DM. TRPA1 is required for histamine-independent, Mas-related G protein-coupled receptor-mediated itch. *Nature Neuroscience.* 2011 May; 14 (5): 595-602.

(96) Elias PM, Nau P, Hanley K, Cullander C, Crumrine D, Bench G, Sideras-Haddad E, Mauro T, Williams ML, Feingold KR. Formation of the epidermal calcium gradient coincides with key milestones of barrier ontogenesis in the rodent. *Journal of Investigative Dermatology*. 1998 Apr; 110 (4): 399-404.

(97) Bikle DD, Ratnam A, Mauro T, Harris J, Pillai S. Changes in calcium responsiveness and handling during keratinocyte differentiation. Potential role of the calcium receptor. *Journal of Clinical Investigation*. 1996 Feb 15; 97 (4): 1085-93.

(98) Darbellay B, Barnes L, Boehncke WH, Saurat JH, Kaya G. Reversal of murine epidermal atrophy by topical modulation of calcium signaling. *Journal of Investigative Dermatology*. 2014 Jun; 134 (6): 1599-608.

(99) Tsutsumi M, Inoue K, Denda S, Ikeyama K, Goto M, Denda M. Mechanical-stimulation-evoked calcium waves in proliferating and differentiated human keratinocytes. *Cell and Tissue Research.* 2009 Oct; 338 (1): 99-106.

(100) Pang Z, Sakamoto T, Tiwari V, Kim YS, Yang F, Dong X, Güler AD, Guan Y, Caterina MJ. Selective keratinocyte stimulation is sufficient to evoke nociception in mice. *Pain*. 2015 Apr; 156 (4): 656-65.

(101) Greig AV, Linge C, Cambrey A, Burnstock G. Purinergic receptors are part of a signaling system for keratinocyte proliferation, differentiation, and apoptosis in human fetal epidermis. *Journal of Investigative Dermatology*. 2003 Nov; 121 (5): 1145-9.

(102) Meşe G, Richard G, White TW. Gap junctions: basic structure and function. *Journal of Investigative Dermatology*. 2007 Nov; 127 (11): 2516-24.

(103) Barr TP, Albrecht PJ, Hou Q, Mongin AA, Strichartz GR, Rice FL. Air-stimulated ATP release from keratinocytes occurs through connexin hemichannels. *PLOS ONE.* 2013; 8 (2): e56744.

(104) Celli A, Mackenzie DS, Crumrine DS, Tu CL, Hupe M, Bikle DD, Elias PM, Mauro TM. Endoplasmic reticulum Ca2+ depletion activates XBP1 and controls terminal differentiation in keratinocytes and epidermis. *British Journal of Dermatology.* 2011 Jan;164(1):16-25.

(105) Menon GK, Elias PM. Ultrastructural localization of calcium in psoriatic and normal human epidermis. *ARCHIVES OF DERMATOLOGY*. 1991 Jan; 127 (1): 57-63.

(106) Bosen F, Celli A, Crumrine D, vom Dorp K, Ebel P, Jastrow H, Dörmann P, Winterhager E, Mauro T, Willecke K. Altered epidermal lipid processing and calcium distribution in the KID syndrome mouse model Cx26S17F. *FEBS Letters*. 2015 Jul 8; 589 (15): 1904-10.

(107) Celli A, Sanchez S, Behne M, Hazlett T, Gratton E, Mauro T. The epidermal Ca^{2+} gradient: Measurement using the phasor representation of fluorescent lifetime imaging. *Biophysical Journal.* 2010 Mar 3; 98 (5): 911-21.

(108) Proksch E, Feingold KR, Man MQ, Elias PM. Barrier function regulates epidermal DNA synthesis. *Journal of Clinical Investigation.* 1991 May; 87 (5): 1668-73.

(109) Denda M, Sato J, Tsuchiya T, Elias PM, Feingold KR. Low humidity stimulates epidermal DNA synthesis and amplifies the hyperproliferative response to barrier disruption: implication for seasonal exacerbations of inflammatory dermatoses. *Journal of Investigative Dermatology*. 1998 Nov; 111 (5): 873-8.

(110) Tsutsumi M, Denda S, Inoue K, Ikeyama K, Denda M. Calcium ion gradients and dynamics in cultured skin slices of rat hindpaw in response to stimulation with ATP. *Journal of Investigative Dermatology*. 2009 Mar; 129 (3): 584-9.

(111) Bikle DD, Mauro TM. Calcium, Orai1, and epidermal proliferation. *Journal of Investigative Dermatology*. 2014 Jun; 134 (6): 1506-8.

(112) Tang EH, Vanhoutte PM. Gap junction inhibitors reduce endothelium-dependent contractions in the aorta of spontaneously hypertensive rats. *Journal of Pharmacology and Experimental Therapeutics*. 2008 Oct; 327 (1): 148-53.

(113) Barbe MT, Monyer H, Bruzzone R. Cell-cell communication beyond connexins: the pannexin channels. *Physiology (Bethesda)*. 2006 Apr; 21: 103-114.

(114) Penuela S, Kelly JJ, Churko JM, Barr KJ, Berger AC, Laird DW. Panx1 regulates cellular properties of keratinocytes and dermal fibroblasts in skin development and wound healing. *Journal of Investigative Dermatology*. 2014 Jul; 134 (7): 2026-35.

(115) Locovei S, Wang J, Dahl G. Activation of pannexin 1 channels by ATP through P2Y receptors and by cytoplasmic calcium. *FEBS Letters*. 2006 Jan 9; 580 (1): 239-44.

(116) Suadicani SO, Brosnan CF, Scemes E. P2X7 receptors mediate ATP release and amplification of astrocytic intercellular Ca^{2+} signaling. *Journal of Neuroscience.* 2006 Feb 1; 26 (5): 1378-85.

(117) Zylka MJ, Rice FL, Anderson DJ. Topographically distinct epidermal nociceptive circuits revealed by axonal tracers targeted to Mrgprd. *Neuron*. 2005 Jan 6; 45 (1): 17-25.

(118) Schäfer-Korting M, Schreiber S. Use of skin equivalents for dermal absorption and toxicity. Roberts, M. S. and Walters, K. A. (eds) *Dermal Absorption and Toxicity Assessment*, Informa, USA. 2008 141-159.

(119) Elias PM. Defensive functions of the stratum corneum: Integrative aspects. Elias PM. and Feingold KR. (eds) *Skin Barrier, Taylor Francis*, USA. 2006 5-14.

(120) Sun R, Anna C, Debra C, Melanie H, Adame LC, Pennypacker SD, Park K,

Uchida Y, Feingold KR, Elias PM, Ilic D, and Mauro TM. Lowered humidity produces human epidermal equivalents with enhanced barrier properties. *Tissue Engineering Part C: Methods*. 2015 Jan; 21 (1): 15-22.

(121) Candi E, Schmidt R, Melino G. The cornified envelope: a model of cell death in the skin. *Nat Rev Mol Cell Biol*. 2005 Apr; 6 (4): 328-40.

(122) Brandner JM, Zorn-Kruppa M, Yoshida T, Moll I, Beck LA, and Benedetto AD. Epidermal tight junctions in health and disease. *Tissue Barriers*. 2015 January-June; 3(1-2): e974451.

(123) Torkamani N, Rufaut NW, Jones L, Sinclair R. Epidermal cells expressing putative cell markers in nonglabrous skin existing in direct proximity with the distal end of the arrector pili muscle. *Stem Cells International*. 2016 May; 2016: 1286315.

(124) Seirin LS. Lateral inhibition-induced pattern formation controlled by the size and geometry of the cell. *Journal of Theoretical Biology*. 2016 Sep; 404: 51-65.

(125) Hagiwara M. An in vitro-in silico interface platform for spatiotemporal analysis of pattern formation in collective epithelial cells. *Integrative Biology*. 2016 Aug; 8 (8): 861-8.

(126) Giangreco A, Goldie SJ, Failla V, Saintigny G. Watt FM. Human skin aging is associated with reduced expression of the stem cell markers beta1 integrin and MCSP. *Journal of Investigative Dermatology*. 2010 Feb; 130 (2): 604-8.

(127) Ghadially R, Brown BE, Sequeira-Martin SM, Feingold KR. Elias PM. The aged epidermal permeability barrier. Structural, functional, and lipid biochemical abnormalities in humans and a senescent murine model. *Journal of Clinical Investigation*. 1995 May; 95 (5): 2281-2290.

(128) Halder G, Dupont S. Piccolo S. Transduction of mechanical and cytoskeletal cues by YAP and TAZ. *Nature Reviews Molecular Cell Biology*. 2012 Sep; 13 (9): 591-600.

(129) Porazinski S, Wang H, Asaoka Y, Behrndt M, Miyamoto T, Morita H, Hata S, Sasaki T, Krens SFG, Osada Y, Asaka S, Momoi A, Linton S, Miesfeld JB, Link BA, Senga T, Shimizu N, Nagase H, Matsuura S, Bagby S, Kondoh H, Nishina H, Heisenberg CP, Furutani-Seiki M. YAP is essential for tissue tension to ensure vertebrate 3D body shape. *Nature*. 2015 May; 521 (7551): 217-221.

(130) Dupont S, Morsut L, Aragona M, Enzo E, Giulitti S, Cordenonsi M, Zanconato F, Le Digabel J, Forcato M, Bicciato S, Elvassore N, Piccolo S. Role of YAP/TAZ in mechanotransduction. *Nature*. 2011 Jun; 474 (7350): 179-83.

(131) Beverdam A, Claxton C, Zhang X, James G, Harvey KF, Key B. Yap controls

stem/progenitor cell proliferation in the mouse postnatal epidermis. *Journal of Investigative Dermatology*. 2013 Jun; 133 (6): 1497-505.

(132) Zhou K, Muroyama A, Underwood J, Leylek R, Ray S, Soderling SH, Lechler T. Actin-related protein2/3 complex regulates tight junctions and terminal differentiation to promote epidermal barrier formation. *Proceedings of the National Academy of Sciences of the United States of America*. 2013 Oct; 110 (40): e3820-9.

(133) Lee MJ, Byun MR, Furutani-Seiki M, Hong JH, Jung HS. YAP and TAZ regulate skin wound healing. *Journal of Investigative Dermatology,* 2014 Feb; 134 (2): 518-525.

(134) Randall MJ, Jüngel A, Rimann M, Wuertz-Kozak K. Advances in the Biofabrication of 3D Skin in vitro: Healthy and Pathological Models. *Frontiers in Bioengineering and Biotechnology*. 2018 Oct; 31 (6) :154.

(135) Guttman-Yassky E, Nograles KE, Krueger JG. Contrasting pathogenesis of atopic dermatitis and psoriasis--part I: clinical and pathologic concepts. *The Journal of Allergy and Clinical Immunology*. 2011 May; 127 (5): 1110-8.

(136) Palmer CN, Irvine AD, Terron-Kwiatkowski A, Zhao Y, Liao H, Lee SP, Goudie DR, Sandilands A, Campbell LE, Smith FJ, O'Regan GM, Watson RM, Cecil JE, Bale SJ, Compton JG, DiGiovanna JJ, Fleckman P, Lewis-Jones S, Arseculeratne G, Sergeant A, Munro CS, El Houate B, McElreavey K, Halkjaer LB, Bisgaard H, Mukhopadhyay S, McLean WH. Common loss-of-function variants of the epidermal barrier protein filaggrin are a major predisposing factor for atopic dermatitis. *Nature Genetics*. 2006 Apr; 38 (4): 441-6.

(137) Fallon PG, Sasaki T, Sandilands A, Campbell LE, Saunders SP, Mangan NE, Callanan JJ, Kawasaki H, Shiohama A, Kubo A, Sundberg JP, Presland RB, Fleckman P, Shimizu N, Kudoh J, Irvine AD, Amagai M, McLean WH. A homozygous frameshift mutation in the mouse Flg gene facilitates enhanced percutaneous allergen priming. *Nature Genetics*. 2009 May; 41 (5): 602-8.

(138) Park BS, Youn JI. Factors influencing psoriasis: an analysis based upon the extent of involvement and clinical type. *Journal of Dermatology* 1998 Feb; 25 (2): 97-102.